



**Statistical characterisation of  
architectural parameters in  
heterogeneous, high-porosity media  
and their influence on the fluid  
properties**

**Jack Waghorne**

Submitted as a partial requirement for the completion of a  
Master of Science (MSc) by research degree in computer  
science, to be awarded by Oxford Brookes University

School of Engineering, Computing & Mathematics (ECM)

Oxford Brookes University

United Kingdom

12/2022

# Abstract

This thesis sets out to uncover the unknown mechanisms that control the complex, heterogeneous function of the meniscus. This has been accomplished through the use of modern pore network extraction (PNE) techniques to characterise the pore space within the meniscus, a soft tissue situated inside the knee which is fundamental for the correct functioning of the joint. While these PNE techniques were not primarily designed for use in high-porosity materials, this project demonstrates that they can be adapted for use in complex biological materials with the inclusion of bespoke adaptations developed in this study. Current literature has highlighted notable variance between results depending on the method selected to segment the pore space. To ensure a fully comprehensive analysis, a selection of three segmentation methods were assessed for comparison. This project found that the choice of the segmentation method does in fact have a notable impact on the characterisation of the pore space and the decision of which method to implement should be dependent on the goal and scope of the study. Pore network modelling (PNM) was initially designed not only for the characterisation of the pore space, but for the prediction of transport properties. As the current literature shows significant inconsistencies in the results of fluid properties, such as permeability, it was decided to employ more stable and trustworthy methods, namely, tortuosity quantification and CFD analysis. Again, to ensure a comprehensive analysis of parameters, three different methods of determining geometric tortuosity have been implemented in this project. These methods each require varying amounts of information from the pore space to function which, as such, affect memory usage, run-time and tortuosity values. The tortuosity analysis demonstrated that the structure of the meniscus creates twofold anisotropy, both in the orthogonal direction and along the Z-Direction. This anisotropic effect was confirmed by the novel approach of coupling computational fluid dynamics (CFD) methods with modern image analysis techniques (CFD-IA). The CFD-IA analysis demonstrated that in CFD simulations, fluid paths orientation between 270-330° along the Z-direction had lower tortuosities than others. This CFD-IA also demonstrated the ability to highlight the potential limitations of PNM and statistically quantify the relationship between architectural parameters and fluid velocity and Reynolds Number.

# Contents

<b>1</b>	<b>Introduction</b>	<b>6</b>
<b>2</b>	<b>Methodology</b>	<b>16</b>
2.1	Image acquisition & pre-processing . . . . .	16
2.2	Segmentation . . . . .	17
2.3	Connectivity . . . . .	22
2.4	Throat Quantification . . . . .	23
2.5	Tortuosity . . . . .	25
2.6	Coupling CFD & Image analysis . . . . .	28
<b>3</b>	<b>Results</b>	<b>31</b>
3.1	Model validation and performance . . . . .	31
3.2	Characterisation of pore space . . . . .	35
3.3	Tortuosity . . . . .	39
3.4	Solid-body Modelling . . . . .	42
3.5	Determination of fluid properties . . . . .	43
<b>4</b>	<b>Discussion</b>	<b>46</b>
<b>5</b>	<b>Appendix</b>	<b>56</b>

# List of Figures

1.1	Introduction into meniscal literature . . . . .	7
1.2	Introduction into tortuosity (Fu <i>et al</i> , 2021) . . . . .	12
2.1	Meniscus samples in-vivo . . . . .	16
2.2	2D $\mu$ CT scan image of meniscus . . . . .	16
2.3	Scan image after binarisation . . . . .	16
2.4	a) 3D image stack with coordinate system b)Names and dimensions of all meniscal datasets . . . . .	17
2.5	Processes of cMBA segmentation . . . . .	20
2.6	Processes of mMBA segmentation . . . . .	21
2.7	Processes of WA segmentation . . . . .	22
2.8	Connectivity analysis . . . . .	22
2.9	Throat quantification process . . . . .	23
2.10	Adapted PNM process (Weisstein, 2007) . . . . .	25
2.11	Voxel-connectivity tortuosity process . . . . .	27
2.12	(a) Visual demonstration of different tortuosity methods through the same sine wave (b) Table describing the true and calculated tortuosities of the sine wave . . . . .	28
2.13	Interpolated speed values . . . . .	29
2.14	Example of segmented pore space . . . . .	29
2.15	Visualisation of equivalent pore diameters . . . . .	29
2.16	Plots of fluid streamlines from CFD simulation . . . . .	30
3.1	Computational time comparison of segmentation methods . . . . .	35
3.2	Pore-size distribution comparison of segmentation methods . . . . .	37
3.3	Connectivity distribution comparison of segmentation methods . . . . .	38
3.4	Throat parameter comparisons of segmentation methods . . . . .	39
3.6	Twofold anisotropy in meniscus samples . . . . .	41
3.7	Tortuosity characteristics of meniscus samples . . . . .	41
3.8	Solid-body modelling process . . . . .	42
3.9	Comparison between global and local Re . . . . .	43
3.10	cfb tort . . . . .	44
3.11	Structural parameters correlation plot . . . . .	45
5.1	Pore-size based on segmentation method . . . . .	56

5.2	Connectivity based on segmentation method . . . . .	56
5.3	Throat-size based on segmentation method . . . . .	56
5.4	Throat length based on segmentation method . . . . .	57
5.5	Tortuosity methodology comparison . . . . .	57

# List of Tables

1.1	Benchmark dataset results from current literature . . . . .	11
3.1	MBA validation comparison table . . . . .	32
3.2	WA validation comparison table . . . . .	33
3.3	Tortuosity validation table . . . . .	34
3.4	Meniscus samples properties . . . . .	36
3.5	Pore sphere collision of solid-bodies . . . . .	42
5.1	Property table of rock paramters calculated using PNM . . . . .	58

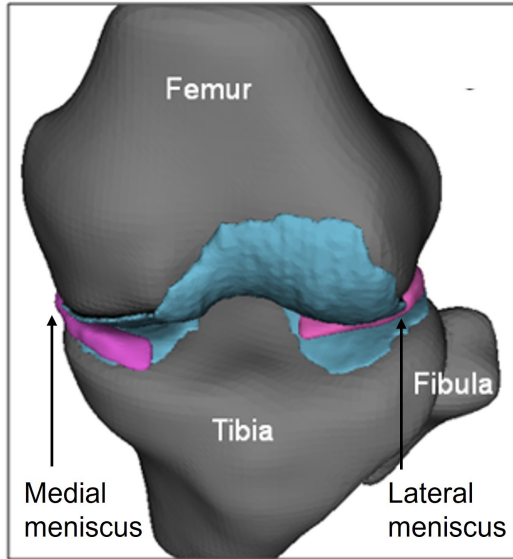
# Chapter 1

## Introduction

### The meniscus

Biological materials, specifically soft load-bearing tissues, present spatially heterogeneous structures [1]. These materials are predominantly biphasic, comprised of a porous solid phase (constituted mainly by collagen) with porosity varying between 50-70% in the internal layers and a liquid phase (water). The human knee contains a multitude of these tissues in tendons and cartilage that allow for bio-mechanical articulation and rotation. The meniscus is the most prominent of these tissues, facilitating load transfer between the upper and lower part of the body from the femur condyles to the tibial plateau [2, 3] (Figure 1.1a). It has been shown that degradation due to ageing or traumatic injuries of the meniscus has a significant effect on contact pressure distribution in the articular cartilage within the knee [4] which can cause the early onset of osteoarthritis (OA). Considering this, it is clear that menisci are critical to the normal function of bipedal movement and that damage or improper function of them can be detrimental to those afflicted [5]. Recent studies have employed a plethora of imaging techniques to better comprehend the structure of menisci [6, 7, 8]. The structure is similar to a sandwich structure with a stiff outside layer and a softer internal layer so that it can accommodate deformation and dissipate energy. This tissue can be seen as an effective damping system designed and optimised by nature. The orientation and patterns fabricated by these fibres are inhomogeneous and change depending on where in the meniscus they are located, circumferentially, radially and vertically [9]. Procedures have been designed [10, 11] to show that the diversity of structures within the meniscus changes the mechanical [8] (Figure 1.1b) and fluid [12] response of the structure. Undoubtedly, this is no mistake, as inhomogeneous structures have frequently been discovered in nature and have been repeatedly shown to explain advantageous characteristics of organisms [13, 14, 15]. Once the nuances of how a structure is designed to accomplish its function are understood, it is then possible to exploit these characteristics, optimise functionality and amend undesirable features. OA is prominent in the modern world, with the primary demographics being athletes [16] and the elderly [17]. This highlights that while the meniscus performs well within a certain usage and time range, degradation and longevity are parameters that desperately need

improvement. Current surgical solutions for knee repair are few, with the main surgical interventions being partial or full meniscectomy, while these operations can provide positive short-term effects, long-term studies found an increase in early-onset OA in full meniscectomy surgeries [18]. Current studies are pioneering the development of biofabrication techniques [19, 20] to produce synthetic tissue samples for application in restorative allotransplantation surgeries [21], however, many of these studies highlight the lack of longitudinal studies due to the novelty of these developments. Many of the meniscal designs of these are just based on crude parameters that, while having value, do not truly replicate meniscal function. Additionally, due to constraints of printing complex natural structures [22, 23, 24], errors are likely to occur. The need is therefore apparent, the development of a comprehensive way to model the complex structure that can not only provide quantitative information about the morphological and architectural properties of the pore space but also offer the robustness to make acceptable simplifications to make manufacturing more feasible.



(a) Structure of the knee generated using CAD (Bulle *et al*, 2021)



(b) Bi-axial mechanical testing of meniscus sample (Waghorne *et al*, 2023)

Figure 1.1: Introduction into meniscal literature

## Pore space characterisation

Over the last 15 years, methods have been devised to quantify, simplify and emulate complex pore spaces, transforming them from uninterpretable labyrinths into systems that can be quantified and evaluated. These methods, such as pore network modelling (PNM), have been growing in tandem with the availability and simplicity of extracting highly quality scan data at the pore scale. Micro-CT ( $\mu$ CT) imaging offers non-invasive and a non-destructive way to capture the internal structure of solid materials. This type of imaging offers flexibility in resolution and sample size, meaning it is utilised in a variety of different scientific disciplines. This flexibility allows for the acquisition

of scans with extremely high resolution (up to 300nm/voxel using synchrotron equipment), but this results in sizeable datasets which are computationally expensive to analyse. Medium-resolution  $\mu$ CT scans (6.25  $\mu$ m/voxel) of a cylinder of the meniscus with a diameter of 1mm and length of 3mm, created an image stack with a file size of over 3Gb. While these datasets still require a notable amount of time to analyse, this resolution was found to be a suitable balance between image clarity and computational requirement.

Originating predominantly in the geosciences, PNM methods were developed to model wettability, hydrology and multiphase flow [25]. These methodologies were quickly adopted by a plethora of disciplines and can now be found in many problems where permeability and fluid properties are of interest; from battery discharge modelling to soil aggregate wettability, PNM has proved to be incredibly robust in its applications. The field of image analysis for the characterisation of architectural parameters of porous media is a constantly evolving landscape [26, 27, 28, 29], this constant advancement means there is substantial subjectivity in regards to what methods are most suitable for characterising a pore space. Most models are validated via comparison of results of fluid properties from the pore network model, such as permeability, with that of experimental values. This is done without much investigation into the stability of results or what factors within the pore network hold the greatest effect. Recent studies have begun investigations into these relationships [30, 31, 32], often with unconsolidated spheres or lattice shapes PNMs, which are not always conducive to real porous structures environments. Many of these studies also solely focus on a select few parameters, most prominently capillary (or 'throat') morphology [30, 31, 33, 34], this is because, as [25] states: "The most basic assumption made is that the flow is capillary dominated (quasi-static) with viscous pressure drops in the model being insignificant in comparison to capillary pressure". This implies that significant care should be taken when characterising throat parameters. Contradictory to this, many studies only stipulate equivalent throat radii using the crude method of counting surface voxels [35, 36, 37, 38] and only in recent has this evolved to include true throat morphology [33, 34]. Ideally, these parameters would be tested on bio-mimetic artificially generated datasets, with tunable control parameters to observe the effects on test parameters. While there is some work into physically informed GAN models such as described in [39, 40], however, this research is still in its infancy and is predominantly limited to 2D. Additionally, while the use of deep learning can effectively produce predictions, these are often seen as a 'black-box' making it difficult to draw conclusions about the true material.

All PNMs are characterised using a pore network extraction (PNE) process, PNE describes a series of algorithms that quantify the porous medium's morphology, topology and architectural features. All PNE processes start with the fundamental step of segmentation of the pore space. Current segmentation methodologies fall into 2 main categories, maximal-ball algorithm (MBA) [35, 41, 42, 43] or watershed segmentation

analysis (WA) [36, 37, 44, 45], the details of which can be found in Section 2.2. As mentioned, these methods were originally designed for use in geological datasets, which are typically low-porosity ( $\leq 35\%$ ) and relatively homogeneous. This prompts the imperative question of if these methods are appropriate for use in biological materials, which have been shown not to possess these characteristics. There are two main factors that are cause for this question:

1. Meniscus samples are of a much higher porosity than typical rock datasets.
2. Tissue systems are formed by a series of gradual biochemical processes, to produce a structure that performs a function, which rock samples are not.

Both of these issues affect the segmentation process, firstly, having a higher porosity leads to more larger pores being created in much closer proximity to each other. This leads to numerous instances of overlapping geometry during the morphology simplification stage (see Section 2.4 for more details). If this overlap is present in locations where pores are not in contact in the true morphology of the pore space, then the PNM will misrepresent the medium, impacting fluid and mechanical properties. Secondly, the fibrous structure of the meniscus could present an obstruction to the segmentation method, the basis of both segmentation methods relies on regions of greater volumes being connected through points of low volume (constrictions). If the fibrous architecture does not converge into these points consistently or if the structure contains more prolate morphology [36], this could potentially disrupt the detection of potential pores. These issues are rarely addressed in the literature, likely because they are uncommon in lower porosity materials as pores are distributed further apart within the sample and throats are generally smaller. Other studies recognise these issues but employ the use of 'idealised' materials [38] which are designed to purposefully avoid these interactions. A scarce number of studies have attempted the characterisation of tissue-like materials, however, a study by [46] has seen success in capturing anisotropic characteristics in biological scaffolds using PNM but this was only accomplished using a distributed sphere approach and did not incorporate any natural morphology. Some studies suggest that popular filtering techniques used in current watershed segmentation are designed for geological samples [36], hindering their performance in fibrous media. These investigations subsequently offer adapted methods to improve this [36, 45]. To compare the effect of the segmentation method and validate results with secondary sources, studies were collated that analysed benchmark datasets. The datasets used are a collection of carbonate and sandstone rock types, which have been acquired and developed by Imperial College London ([47] [48]) and characterised using the both MBA and WA methods ([33, 35, 41, 42]). The only exception to this is the Bentheimer and Estillades datasets which were analysed by [41]. The inclusion of these datasets was in part for additional variation in data, the Bentheimer data in particular is of significantly larger size ( $1000 \times 1000 \times 1000$ ), being over double that of the next largest dataset. While these benchmark datasets have been rigorously evaluated for morphological and fluid flow characteristics, very few of these studies have conducted topological analysis, as

this parameter tends to be quite separate from the PNM methodology. Therefore, for the validation of tortuosity, an additional 5 datasets were acquired. These datasets were developed by [49] and evaluated for topological properties in [50]. A table for the review and later comparison of all these results found in the current literature can be seen in Table 1.1.

Sample	Resolution n	Porosity (%)	No. Pores			No. Throats			Avg. Pore Diameter ( $\mu\text{m}$ )			Avg. Throat Diameter ( $\mu\text{m}$ )			Avg. Coordination Number			Tortuosity			
			cMBA	mMBA	WA	cMBA	mMBA	WA	cMBA	mMBA	WA	cMBA	mMBA	WA	cMBA	mMBA	WA				
Berea	5.35	19.6	6298	7611	-	12545	14328	-	30.72	33.58	52.44	14.30	18.18	29.40	143.7	99	112.98	3.98	3.77	2.90	-
C1	2.85	23.3	4576	4115	-	6921	8893	-	14.1	17.32	22.78	8.04	9.02	23.98	88.4	82.8	62.49	3.02	4.32	2.12	-
C2	5.35	16.8	8508	5590	-	10336	11654	-	22.78	29.24	36.00	12.34	14.78	30.20	122.8	100.10	94.29	2.43	4.14	1.55	-
S1	8.68	14.1	1868	1452	-	3048	2455	-	51.18	65.18	98.36	24.64	33	49.76	232.6	204.2	207.04	3.26	3.38	2.64	-
S2	4.96	24.6	2021	2906	-	4942	5792	-	34.50	36.10	61.28	16.26	19.58	32.44	154.9	103.5	120.13	4.89	3.99	3.80	-
S3	9.10	16.9	8926	9104	-	15105	15833	-	33.38	39.84	65.10	15.02	20.44	28.52	161.5	117	143.84	3.38	3.48	2.49	-
S4	8.96	17.1	9556	7199	-	13322	11508	-	33.60	41.80	65.36	15.62	21.2	30.98	151.1	121	133.83	2.79	3.2	2.07	-
S5	4.00	21.1	518	659	-	1243	900	-	33.42	35.68	52.14	18.98	18.72	43.70	187.00	122.50	128.81	3.47	3.77	2.45	-
S6	5.10	24	597	1022	-	1234	2147	-	38	37.58	66.66	20.20	19.68	53.46	229.20	144.60	145.57	4.13	4.20	3.23	-
S7	4.80	25.1	1016	1759	-	2741	3448	-	40.3	38.02	70.22	18.60	20.80	37.90	187.30	115.50	138.38	5.40	3.92	4.11	-
S8	4.89	34	1324	2439	-	4209	5235	-	42.32	39.64	54.32	20.94	22.32	42.48	194.40	123.00	126.60	6.36	4.29	3.56	-
Estallades	3.30	12.2	2500	2612	-	-	-	-	-	-	-	-	-	-	-	-	-	4.60	2.60	-	-
Bentheimer	3.00	21.6	10377	18535	-	-	-	-	-	-	-	-	-	-	-	-	-	3.60	2.9	-	-
F8	5.70	8.6	-	-	-	-	-	-	-	-	-	-	-	-	-	-	-	-	1.91	-	-
F10	5.70	10.2	-	-	-	-	-	-	-	-	-	-	-	-	-	-	-	-	1.76	-	-
F13	5.70	12.6	-	-	-	-	-	-	-	-	-	-	-	-	-	-	-	-	1.57	-	-
F15	5.70	15.4	-	-	-	-	-	-	-	-	-	-	-	-	-	-	-	-	1.46	-	-
F18	5.70	17.6	-	-	-	-	-	-	-	-	-	-	-	-	-	-	-	-	1.4	-	-

Table 1.1: Benchmark dataset results from current literature

## Tortuosity

Tortuosity is a parameter that for decades has been used for explaining fluid transport properties in porous media. Empirical formulations such as the Bruggeman correlation [51] unify together the inherent relationships between porosity, tortuosity and permeability [52]. Tortuosity is a dimensionless measurement that is used to describe the amount of topological resistance a fluid will encounter while travelling through a medium. This relationship is described by calculating the ratio of path length traversed by the fluid, by the straight-line distance between the start-finish point (SFP) of the path, or to putting this into an equation:

$$T = \frac{L_t}{L_e} \quad (1.1)$$

Where  $T$  is the tortuosity of the path,  $L_t$  is the length of the traversed path and  $L_e$  is the straight line distance between the SFP, equal to the euclidean distance of between the points. While this seems very simple in theory, there is a rampant lack of standards when it comes to definitions [53], method selection [50, 54] and selection of SFPs [55]. What's more, tortuosity is not always isotropic through a medium, material parameters such as porosity, connectivity and morphology [56] affect tortuosity, if these parameters are spatially heterogeneous, such as in menisci, then the tortuosity can become anisotropic [57, 58].

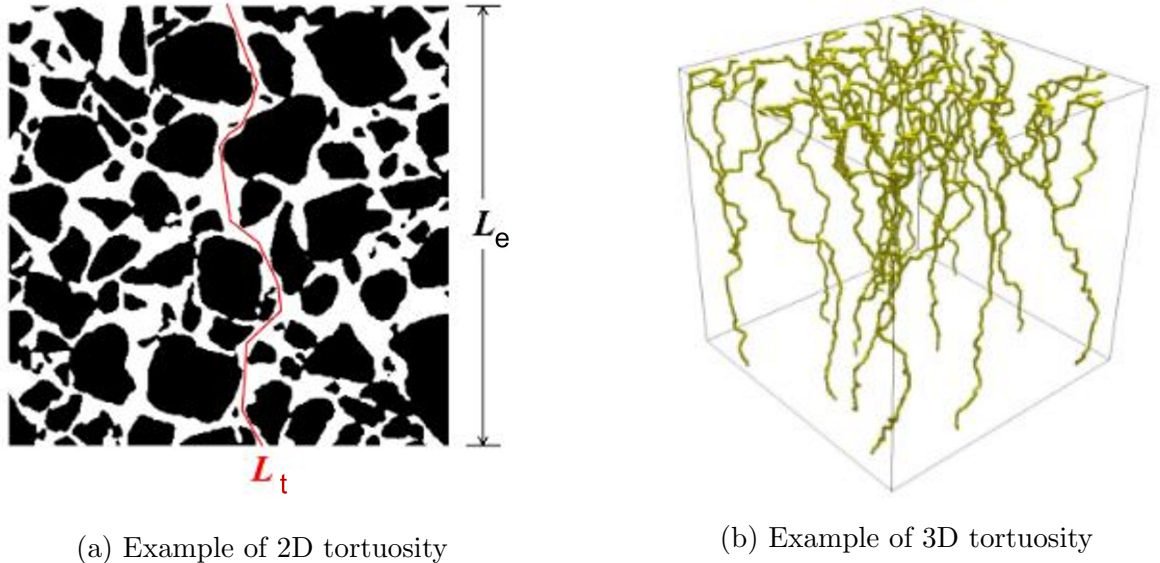


Figure 1.2: Introduction into tortuosity (Fu *et al*, 2021)

## Fluid flow properties

As discussed previously, the common goal of these studies is to derive transport properties, such as permeability, this is accomplished using either 'direct' or 'indirect' methods. Indirect utilises assumptions and algorithms to simplify features of the pore space

down to easily interpretative models. Examples of these methods include the aforementioned PNM which is more of the research standard but other models do exist, such as the 'bundle-of-tubes' model [59, 60] which could prove more informative given the tubular structure of the meniscus. For the scope of this project, however, only PNM will be considered. Characterisation of the pore space is a necessary step in the process of indirect methods, with studies making considerable assumptions about throat morphology transport properties, such as the flow inside the system being Darcian, laminar flow. The assumptions initially made on throat morphology were considered crude, which resulted in the overestimation of properties such as permeability, compared to practical experiments [35, 61]. These methods have been improved over time by the addition of non-uniform throat geometry [34]. However, few studies have ever thoroughly investigated the validity of the assumptions made on the flow regime. Studies that have, have shown that local pore-scale features can impact the flow regime [32], however, the assumption of laminar flow has never been truly challenged. Direct modelling methods include Computational Fluid Dynamics (CFD), Finite Element (FE) [62, 63] and Lattice Boltzmann Method (LBM) [64, 65]. These methods allow for the direct solving for flow properties numerically using Navier-Stokes equations. Direct methods like CFD offer an attractive and robust way to calculate fluid properties within a system and their long-term usage demonstrates that results are reliable, without the need for excessive assumptions on the flow properties. Unfortunately, one of the prominent issues with CFD modelling is meshing. In mediums with highly complex morphology, such as in menisci, meshing is exceptionally difficult as tight or sharp morphology requires highly irregular mesh cells to be constructed. Not only are degenerative mesh cells difficult to identify and fix, but even irregular non-destructive cells can cause issues in simulation, leading to anomalous results. PNM could potentially be a solution to this problem, as solid-body geometry can be extracted from pore network models, which only feature smooth, regular geometry, simple for meshing. New state-of-the-art methods have begun using a semi-analytical combination of both direct and indirect methods [33, 34, 66]. All of these studies couple the two methods using LBM for the purpose of improving calculation time. While the improvements these methods accomplish are impressive, they do possess considerable limitations. These bespoke hybrid-LBM methods are notably difficult to implement and require considerable knowledge of mathematical modelling and computer programming to implement. CFD software offers the same physically informed CFD modelling as LBM, with a significantly more user-friendly interface and less extensive knowledge requirement. Therefore, a method that can combine direct and indirect methods using these software is highly desirable. Unfortunately, most CFD software do not inherently possess the ability to conveniently couple the fluid properties with morphological or topological information. Without this structural information, it is difficult to draw meaningful conclusions as to why transport parameters are valid and what mechanisms control this, providing only causation without correlation. For example, it is possible to locate regions of high fluid velocity in CFD simulations, but it is the task of the user to draw

meaningful conclusions as to why these occur and with the limited structural information provided by the software this can be a perplexing task. Coupling direct CFD methods with indirect pore-scale image analysis techniques could provide answers to the questions posed above. For these CFD - image analysis (CFD-IA) methods to be convenient and easily adoptable they should be developed using CFD software, but allow for the extraction of morphological and topological information.

## Objectives & structure

This chapter has highlighted a litany of questions that must first be answered before the valid characterisation of meniscal pore space and, hence, the manufacturing of truly bio-mimetic meniscal implants can be conceived. This chapter has posed many queries, which have been condensed into 6 primary research questions (RQ):

**RQ1:** Is pore network modelling suitable for the characterisation of high porosity biological media?

**RQ2:** Which segmentation method is most applicable to the fibrous structure of meniscal tissue?

**RQ3:** Are pore network models capable of accurately predicting fluid transport properties in the meniscus?

**RQ4:** Which method of determining geometric tortuosity should be selected for reflecting true fluid paths?

**RQ5:** Is it possible to use CFD-IA coupling extract meaningful information about fluid properties?

**RQ6:** Can we infer from the information gathered how the meniscus is structured to optimise its function?

To answer these crucial questions would mean the advancement of the current knowledge in a number of ways. The most prominent advancements this project demonstrates are:

- The testing of multiple pre-processing and filtering techniques for meniscal scan data.
- A thorough examination of current segmentation methods and their effects on results and performance.
- Novel adaptions made to existing PNM methods to make them applicable for use in modelling high-porosity media.
- Testing, comparison and validation of unexplored tortuosity determination methods.
- Use of a novel methodology to couple direct and indirect methods for determining fluid properties.

- Identification of potential roles played by structural elements of the meniscus to accomplish its function.

This project has been structured as shown below to clearly demonstrate the relevant steps taken to draw the conclusions made by this project.

- Presentation of the low-resolution ( $\mu$ CT) scans, briefly discussing how the samples were extracted from the main body of the meniscus and a demonstration of how these were used to created 3D volumetric data within MATLAB.
- Explanation and rationale of all pre-processing steps performed on the scans before undergoing analysis.
- The full workflow for statistical characterisation of the pore space, including: Segmentation, connectivity analysis, throat quantification and tortuosity determination.
- A brief overview of the numerical CFD experiments, followed by an explanation of how the results of the experiments are coupled with image analysis in a novel way.
- Validation, presentation and dissemination of results from pore space characterisation and CFD-IA coupling.
- Discussion on results, rationalising and describing the conclusion drawn from the results of the project.

# Chapter 2

## Methodology

### 2.1 Image acquisition & pre-processing

This project utilises a series of  $\mu$ CT scan-images of the complex heterogeneous meniscus sample, such as the one seen in Figure 2.2. Further details about the scanner used (Skyscan 1272, Bruker Kontich, Belgium) along with the scanning process can be found in [6, 39]. The end result of these scans is 4 unique datasets taken from nearby sections of the same meniscus sample, taken from the main body of the meniscus, as can be seen in Figure 2.1. The datasets have been uniquely labelled for identification during analyses, the dimensions of which can be seen in Figure 2.4b. The grayscale image stacks were then imported into MATLAB and combined to create a 3D volumetric image (Figure 2.4a). It is essential to have clearly defined boundaries between pore and material phases in the image during analysis, this is accomplished through a binarisation process using thresholding. A threshold was created using an adaptive binarisation function built into MATLAB, the 'adaptive' feature of the function pertains to the incorporation of local differences in luminance values when creating a threshold, the results of which can be seen in Figure 2.3. This was chosen over the 'global' method, which creates a threshold value using Otsu's method. This was a design choice as Otsu's method is seen to perform sub-optimally when the discrepancy between the background and foreground is not distinct, which is the case around the peripheries of the pore. The difference created between the two thresholding methods was evaluated and it was found that the global threshold increases the sample porosity by 4% on average. The now binary image then underwent a



Figure 2.1: Meniscus samples in-vivo

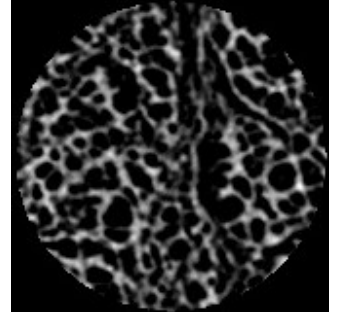


Figure 2.2: 2D  $\mu$ CT scan image of meniscus



Figure 2.3: Scan image after binarisation

'majority' transform, this transformation removes voxels that have less than half of their neighbouring voxels in the pore phase. This process smooths out rough surfaces and plateaus [36] within the model which can interfere with segmentation [37]. Lastly, small pockets of either material or void space are removed through a series of morphological image opening and subsequent closing processes using a spherical structural element with a radius of 2.

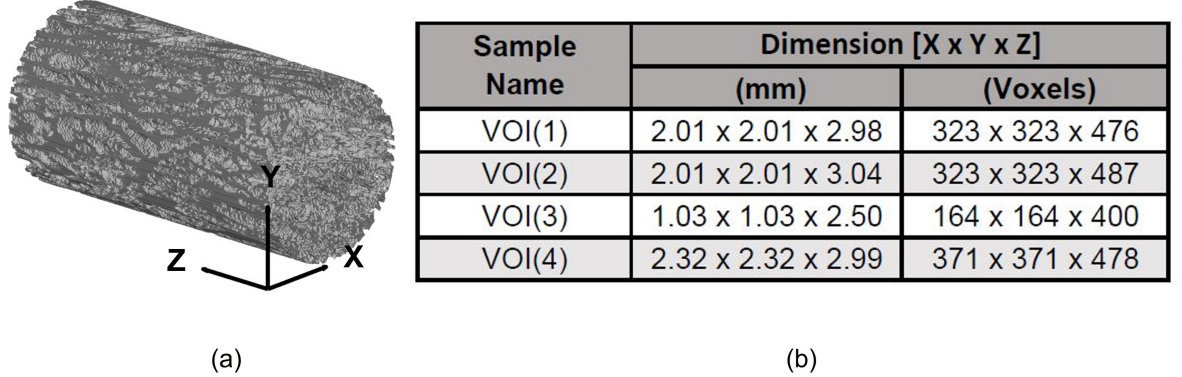


Figure 2.4: a) 3D image stack with coordinate system b)Names and dimensions of all meniscal datasets

## 2.2 Segmentation

These segmentation algorithms, along with all the other PNE algorithms used during this project can be found in [67] for individual inspection. This chapter describes, in detail, the rationale and processes associated with each aspect of PNE for visual and logical understanding.

### Classical Maximal-Ball Algorithm

The classical Maximum Ball Algorithm (cMBA) was first introduced by [68] and later popularised by [35]. Whereby the complex morphology of the pore space is described using simple, repeated geometries. Theoretically, any geometry can be used, but the vast majority of studies use spheres due to their ability to contour into smooth edges and having pre-existing infrastructure for application readily available in most programming software. The spheres are created (as is the case with all the following segmentation methods) using a distance transform [69]. The value at each voxel in a distance transform represents the euclidean distance from that voxel to the nearest material phase interface. A helpful way of visualising this transformation is that each voxel has a corresponding sphere attached to it, the sphere is then inflated uniformly to the point where it contacts a material phase interface. Once this occurs the sphere can no longer inflate and this is the value assigned to voxel, corresponding to the radius of the sphere. To help the visualisation of a distance map and 2D example can be seen in Figure 2.5a. The values are largest inside the centre of the volume and gradually decrease approaching the interface (black pixels), demonstrating that only smaller

spheres are able to be formed. With this concept of distance maps in mind, one can imagine that if all these spheres were actually placed within this volume, there would be large amounts of overlap. This overlap between spheres provides very little additional information and the majority of the information about the pore space morphology can be described by only the largest spheres within the volume. Decreasing the number of spheres is imperative to decreasing the computational cost and increasing the speed of the segmentation process, hence, only the largest spheres should be considered. The largest sphere within a region is defined as a sphere whose centroid is not contained within the radius of a larger sphere. Given a situation with two spheres( $i$  &  $j$ ) where the radius ( $r$ ) of  $i$  is larger than  $j$ :

$$r_i > r_j \quad (2.1)$$

Sphere  $j$  will be removed if the euclidean distance between the sphere centres( $L_{ij}$ ) is less than  $r_i$ , shown by the equality in Equation 2.2

$$r_i > L_{ij} \quad (2.2)$$

This process of removing redundant spheres is repeated for all voxels until the only spheres which give the highest amount of information remain is more commonly known as the Maximal-Inscribed Spheres (MIS) as described in [41, 42]. Implementing the aforementioned MIS algorithm is relatively straightforward. One key point that should be mentioned, however, is that this algorithm is highly influenced by sample size, porosity and morphology. To explain the first two points, the more void voxels to interpret, the more calculations must be performed, leading to an increase in computation time. A relationship between sample size and computation time can be seen in Figure 3.1. The last point refers to how many 'corners' the morphology contains, for every small crevice that cannot be reached by a larger sphere, a smaller sphere must be placed. The natural smooth curves within the morphology of the meniscus allow for many of these crevices to occur, leading to a disproportionate amount of smaller spheres. In all the samples, after performing the MIS algorithm, it was found that 80% of all spheres remaining were of radius 1 (directly in contact with a material voxel). This majority of spheres is what contributes to the enormous computation time necessary for this section of segmentation. As these spheres have a radius of 1, by definition they cannot contain the centroid of another sphere and is unlikely to be contained by a larger sphere. It was therefore decided on these grounds to exclude the interpretation of spheres with a radius  $\leq 1.5$  during the MIS - drastically reducing the computation time. Other studies increase this minimum radius value [38], 1.5 was chosen for this project as spheres above this value were seen to be significant during testing. The complex morphology and high porosity of the meniscus means that MIS can take an excessive amount of time if the proper precautions are not taken. The following points have been identified as key techniques for reducing the computation time of the MIS:

1. To reduce the initial number of spheres, only every other sphere should be interpreted, this frequency can be increased or decreased depending on sample

parameters.

2. Spheres of radii  $\leq 1.5$  should not be considered due to their abundance and lack of information.
3. All spheres should be listed in descending size order and evaluated in said order, this prevents redundant calculations on spheres that will be removed.
4. Only voxels contained in the bounding box (Figure 2.5b) of the sphere (bounding box limits are equal to the radius of the largest sphere in the set). This drastically reduces the time and memory required per evaluation.
5. Redundant spheres should be removed dynamically during each evaluation. This immediately reduces the data size and reduces computation for future calculations.

Now that the maximal inscribed spheres have been selected, the segmentation algorithm, cMBA, can be used. This algorithm is used to constitute the boundaries of pores, also known as pore ‘families’. The term families is used due to the hierarchical structure employed by the algorithm, describing a pore chain spanning from a single large ‘parent’ sphere (1st generation) and increasing in generational rank along the chain. The steps of the algorithm can be summarised in the following points:

1. Spheres are categorised into groups by radii and ranked in descending order.
2. All spheres are initially assigned a pore family of 0 and a generation rank of infinity.
3. The spheres in the group being evaluated are sorted in ascending order by their generational rank. This ensures that connected spheres are evaluated before creating new, unnecessary pore families.
4. For the sphere being evaluated there are two possible outcomes depending on the current condition of the sphere:
  - If the sphere has no assigned family, a new family is created and assigned to the evaluated sphere and its generational rank is assigned to 1. All unassigned connected spheres are also assigned to the family and given a generation of 2.
  - If the sphere has already been assigned, all unassigned connected spheres are assigned the family of the evaluated sphere and given a generational rank +1 than that of the current generation of the current sphere.
5. New values of family and generation are stored back in a master list for later interpretation.
6. once a sphere is assigned it cannot be changed, even if contacted by a sphere of an opposing pore family.

The final step in this segmentation process is to fill in the remaining small-radius voxels that were not interpreted in the previous algorithms. This is accomplished using another distance transform, making use of MATLAB's built-in optional output of a label matrix to locate the voxels' nearest interpreted neighbours and subsequently join them to the family of this neighbour. This method is fast and efficient, removing the need for iterative region-filling algorithms [38]. As these voxels mostly appear on the fringes of pores, the macroscopic properties of each pore remain relatively constant, however, this step allows for the retention of the true morphology of the medium so the model is not hindered by any geometrical simplifications. This segmentation method is tried and tested and, while computationally tedious (as discussed in [43]), provides consistent results for pore coordination number [35]. An example of the MBA algorithm can be seen in Figure 2.5c where each pore family has a unique corresponding colour.

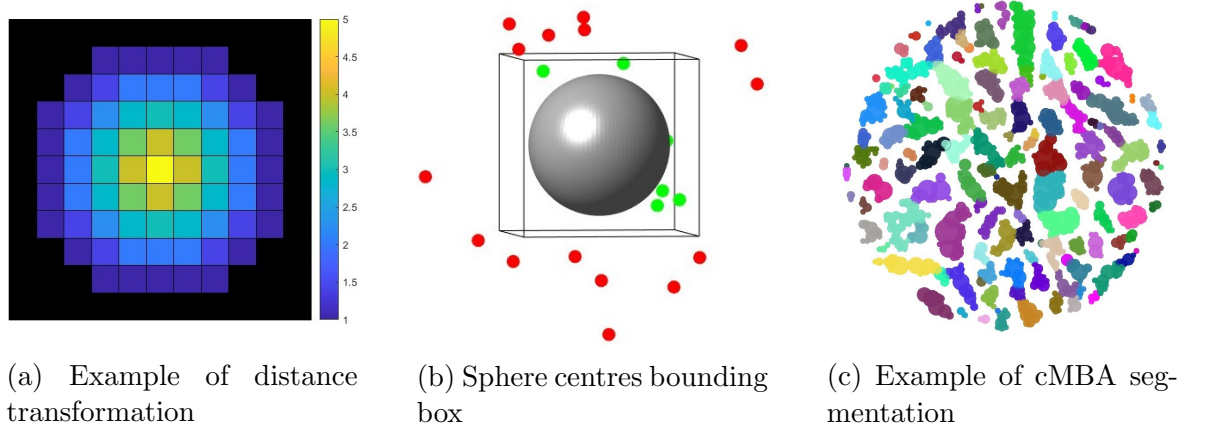
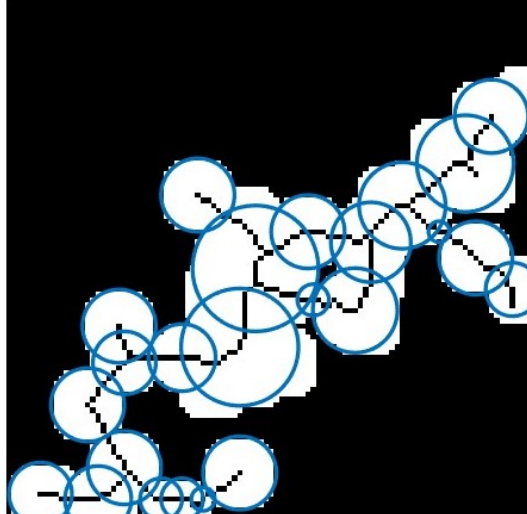


Figure 2.5: Procceses of cMBA segmentation

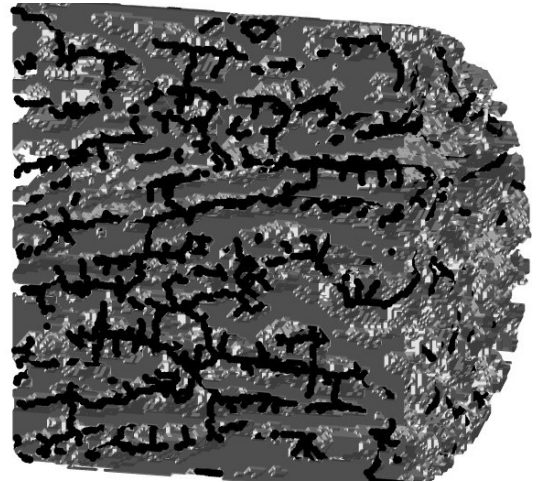
### Medial-Axis

Due to the immense computational cost to interpret the majority of void voxels individually such as in the cMBA, methodologies have been developed to still incorporate the use of maximal balls, but reduce the number of necessary calculations required. This is accomplished by the employment of thinning algorithms such as a medial axis transform [70], this algorithm creates a skeletonised path running through the centroid of the pore space [71] as can be seen in Figure 2.6b. Before creating this skeleton, the datasets must be filtered to remove any pockets of floating material matter in the pore space, which for the most part have been removed during the pre-processing steps in Section 2.1. Failure to do this will result in 'loops' in the skeleton, disrupting the continuity of the path. This skeleton is created in such a way that it runs through the most expansive sections of the pore space, we can conclude that this is likely where the largest spheres will be generated from the distance transform of the pore space. With this in mind, if instead the spheres are built solely on the voxels of this skeleton [42], rather than all void voxels, it is possible to capture the majority of the information of the pore space whilst drastically reducing the number of necessary calculations and guaranteeing continuity throughout the pore space. After this unique step, the mMBA

and cMBA are identical. The spheres undergo the MIS algorithm to remove redundant spheres, an example of which can be seen in Figure 2.6a, and then the MBA defines pore family chains. The families are then dilated to fill the remaining pore space using the same method as the cMBA. This method reduces the amount of computation time by 60-75% depending on sample size.



(a) 2D Example of MIS using mMBA



(b) Visualisation of 3D medial-axis in meniscus

Figure 2.6: Processes of mMBA segmentation

## Watershed

Watershed segmentation differs from the aforementioned methods as it does not describe the pore space by simplifying the topology down to a collection of constrained shapes. Instead, it employs a theory of topological 'catchment basins' [37] which analyses the distance map and creates boundaries along the minima line between local maxima, also known as a 'ridge line'. This analogy of catchment basins can be explained by the following: If the value on a distance map represents the depth of a surface, then the ridge line is created along the boundary where the two basins will spill into each other. This method is desirable as it is remarkably faster than the more traditional MBA methods as seen in Figure 3.1. A downside of this method, however, is that it is susceptible to over-segmentation. To minimise this, steps are taken in the pre-processing stage, such as using filtering to avoid the detection of prolate shapes [38]. This filtering can be done in different ways, most commonly median filtering is employed in [37], however, others argue that it is not beneficial for fibrous media [36]. Methods for fibrous material employ a gaussian filter followed by a series of algorithms to remove local maxima that do not reach a set criterion [36] and then segments using a marker-based watershed method [44, 45]. Due to limitations with marker-based watershed capabilities within MATLAB, it was decided to choose a simplistic median filter, however, gaussian filtering was implemented without the additional steps. This resulted in the gaussian filtering creating 10x the amount of pore families on average, which is vastly over-segmented.

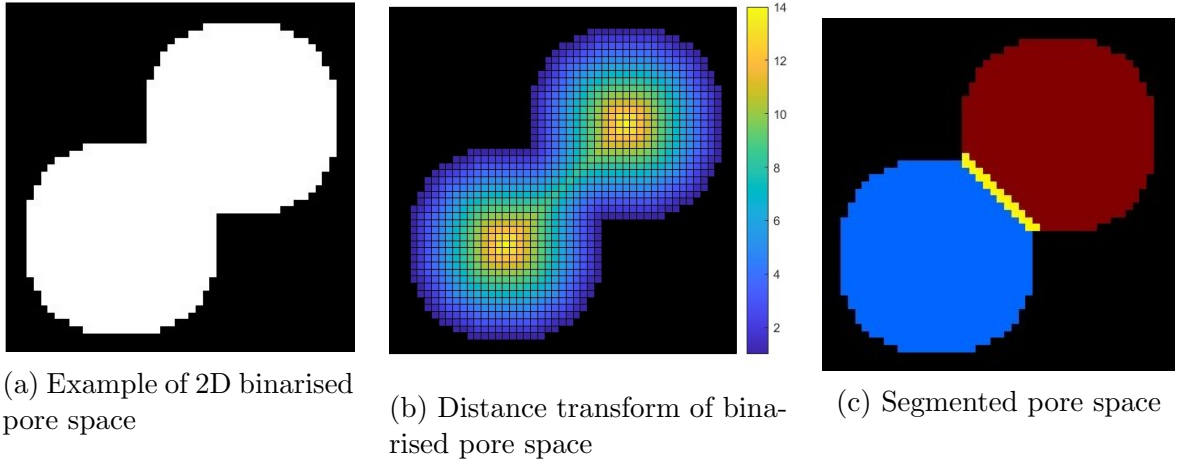


Figure 2.7: Processes of WA segmentation

## 2.3 Connectivity

After segmentation, all processing methods remain constant, regardless of what segmentation method was used, making for a consistent comparison between the results of the models. Connectivity is one of the key parameters of describing a pore network, dictating the number of available pathways for the fluid to take and directly affecting parameters such as tortuosity. As such, great care should be taken when analysing and quantifying network connectivity. The base principle when quantifying connectivity is, if two opposing pore families have neighbouring voxels (Figure 2.8a), they are connected. Popular current methodologies, such as that seen in [38], use image dilation. The methodology used in this project was a voxel-connectivity (VC) based approach, for more details on VC look to Section 2.5. The neighbourhood of every surface voxel is evaluated and voxels that have neighbours of two opposing families are selected as boundary voxels (Figure 2.8b). These boundary voxels are then subtracted from the pore family and stored for throat quantification analysis. This method is robust as it allows control over the volume of the boundary, higher VC will create larger volumes as more voxels are connected, which has a direct impact on the predicted size of throats, this study used a VC of 26 to give the most comprehensive results.

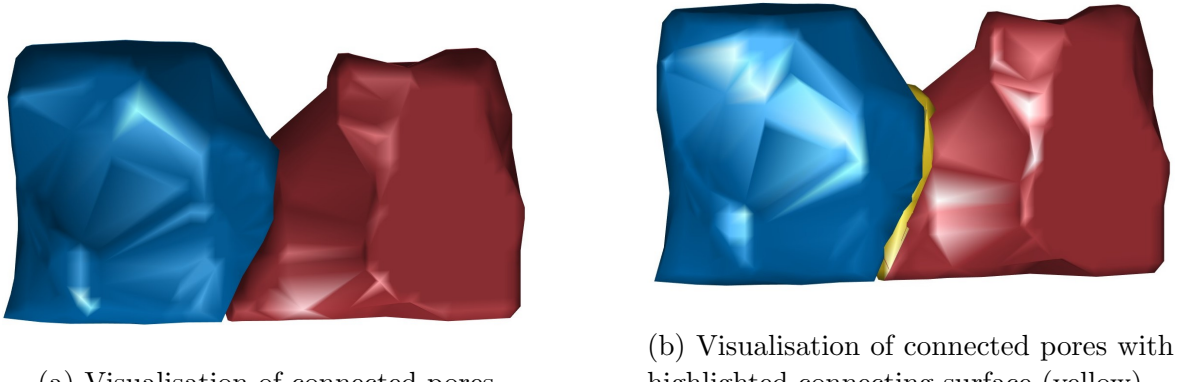


Figure 2.8: Connectivity analysis

## 2.4 Throat Quantification

Storing the boundary voxels during the connectivity analysis allows for the quantification of the throat radii, a critical parameter for the effect of fluid flow in a medium [72]. As stated in [38], the cylindrical throat that will replace the morphology must possess the same cross-sectional area (CSA) as the natural morphology, to preserve porosity [37]. This is a deceptively simple task, as it must be the CSA of the throat normal to the orientation of the connection. Quantifying this is accomplished using a method inspired by [33], in which the 3D boundary volumes are projected onto a 2D plane. These volumes are projected via a sliding plane that is normal to the vector connecting the two centroids of the pores. This plane then slides along the vector at set intervals proportional to the distance between the centroids and takes a 'snapshot' of the voxels orientated in the desired reference frame. These snapshots are then compiled to create a new 3D dimensional volume in the orientation of the connection. As mentioned before, it is not a volume that is required, but an area. Therefore, volume is condensed into a 2D plane taken from the perspective of viewing directly down the orientation of the connection. The CSA is then calculated for the entire closed area, this CSA is then used as an input to find the radius of the equivalent circle ( $r_e$ ) with the same CSA using equation 2.3.

$$r_e = \sqrt{\frac{CSA}{\pi}} \quad (2.3)$$

Depending on the size of the sample and the number of connections this can be a lengthy process so the following tips are advised to reduce the error:

1. Use a square plane with the size of the largest dimension of the bounding box of the volume, to avoid excessive plane sizes.
2. The step size of the plane snapshots should be proportional to the distance between the two centroids. More distant pore centres require more planes to capture all details.

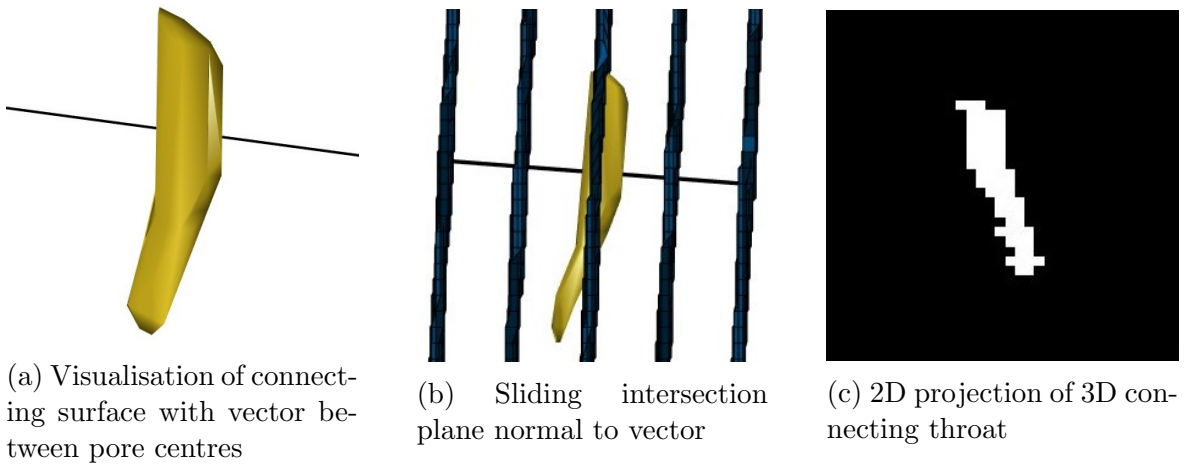


Figure 2.9: Throat quantification process

## Volumetric Modelling

As discussed in Chapter 1, there is a higher risk for potential errors prevalent in the solid modelling of PNMs in mediums with higher porosity than in low. The two main issues are throats having an equivalent radius larger than that of the equivalent radius of one or both of its constituent pores, making for impossible geometries, and pore spheres overlapping. Firstly, it is important to note that overlapping pore spheres of connected pores only become an issue when the overlap has a radius larger than that of the connecting throat. For example, looking at the example in Figure 2.10a, while this overlap appears that it will affect flow properties, if a cross-sectional view of this overlap is viewed such as in Figure 2.10c, then it is seen that the smallest point throughout the connection is still the throat. Therefore, any radius of overlap is arbitrary, provided it remains lower than the radius of the connecting throat. This gives rise to the idea that overlapped connected pores only need to be reduced enough to meet this criterion, it can be checked if a pore pair reaches this criterion with equation 2.4, where R and r represent pore radii and d represent the euclidean distance between them [73] (Figure 2.10b).

$$a = \frac{1}{2d} \sqrt{4d^2R^2 - (d^2 + R^2 - r^2)^2} \quad (2.4)$$

While these issues are not relevant when calculating fluid flow properties analytically, they are when it comes to creating a solid body for meshing. To overcome this issue, a bespoke algorithm was developed to eliminate these geometric discontinuities. The algorithm steps are as follows:

1. All impossible pore-throat geometries (larger throat radius than pore) must be amended by increasing the radius of afflicted pores to match that of their constituent throats.
2. A measure of pore radius 'float' is calculated by subtracting the current radius of the pores by their constituent throat. This float dictates the amount a pore radius can be reduced before it becomes a geometric discontinuity.
3. A pore is evaluated to interpret which pores it is in contact with and by what amount they are overlapped.
4. These overlap values are compared with connecting throat radii, if any overlaps are found to be equal to or lower than connecting throat radii, they are removed from evaluation. For any remaining pores that do have connecting throats, the overlap is subtracted from the throat radius to yield the necessary amount of reduction, any overlaps without connecting throats are set to 0, indicating there cannot be any overlap.
5. These overlap values are then sorted from smallest to largest, the sphere with the smallest overlap value is then selected for shrinkage along with the sphere being evaluated.

6. Depending on the float values and distance of overlap there are four potential outcomes of this step:
  - If both of the pores contain a float value larger than half the distance of overlap: Each of the pores are shrunk by half the distance of overlap
  - If one or more pore has a float value less than half than that of the distance of overlap: The sphere with the smallest float is shrunk as small as possible, to begin with. The remainder of the overlap is then accounted for by shrinking the sphere with the largest float.
  - In the event that both spheres have a float value less than half that of the overlap distance: Both spheres are shrunk to their minimum pore size. The overlap in this instance is unavoidable.
7. Irrelevant of the outcome, new float values and radii are calculated for all spheres altered, these values are reflected in all future evaluations.
8. This process is then repeated for all spheres until all remaining spheres are reduced by the minimum amount to avoid contact or unavoidable contact is made

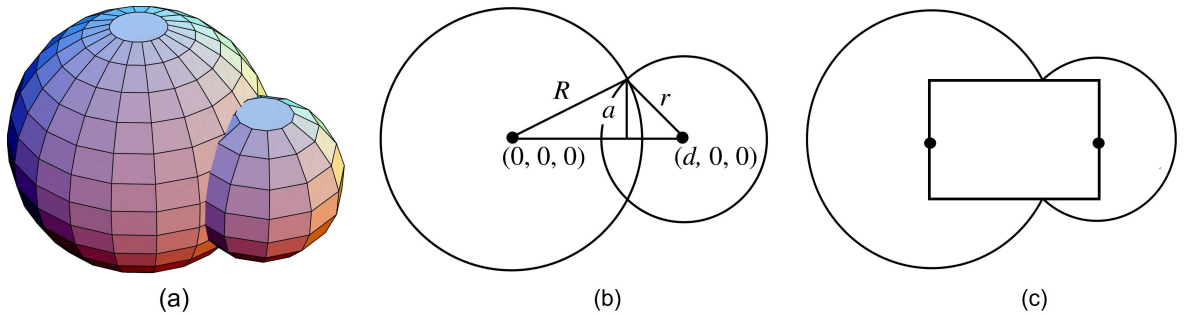


Figure 2.10: Adapted PNM process (Weisstein, 2007)

## 2.5 Tortuosity

To evaluate the variability of tortuosity in high porosity media, three different methods were selected for comparison. Each of these methods were strictly defined in accordance with [53] to promote the use of standards that much current research lacks. In addition to evaluating tortuosity in the assumed fluid direction, the tortuosity has also been evaluated in all orthogonal directions, in all of the methods presented. In instances where a path is not traversable due to a lack of connectivity in the pore space, these results are discarded and not evaluated during any analysis. A brief evaluation of the three tortuosity methods was conducted using a sine wave with small amounts of noise added to allow for segmentation. A visual demonstration of this evaluation can be seen in Figure 2.12a. A sine wave was selected so that the true path length and hence tortuosity could be calculated, the results of which can be seen in Figure 2.12b. As

can be noted in the table, the skeletonised and true path match almost perfectly, while the voxel-connectivity under-predicts and the PNM over-predicts the true value.

## Selection of Start/ Finish nodes

The selection of start and finish points (SFP) is a critical parameter when calculating tortuosity, as each SFP creates a unique path with an associated tortuosity. In the paper by [50], every voxel on the starting plane that has a corresponding voxel in the same position on the finished plane is evaluated. Utilising this method in the meniscus sample is flawed for a few reasons, firstly, as discussed in Chapter 1, studies have found these channels to be orientated in a direction, therefore evaluating only straight-line tortuosity would ignore this potentially crucial part of meniscus function. Secondly, the high porosity of the meniscus means that evaluating all voxels on the start and finish planes drastically increases memory and computational costs, additionally, as the voxels are frequently clustered, many of these paths would be redundant. For these reasons, a new methodology was devised, utilising aspects of the segmentation processes discussed in Section 2.2. First, the sample is segmented 3 dimensionally or the start and finish planes are segmented 2 dimensionally. The centroids of all segmented pores on the start and finish plane are collected, an example of this can be seen in Figure 2.14. Each start pore is paired with every finish point, so the number of unique paths can be calculated by equation 2.5. The benefits of this are twofold, by selecting only the pore centres it can be concluded that SFP are positioned in spatially significant regions and pairing all SFP allows for full orientational analysis in any direction interpreted.

$$N_p = N_s \times N_f \quad (2.5)$$

## Orientation Analysis

In order to detect preferential orientations in the flow direction it is necessary to have a quantitative measure of which direction the flow is travelling. To do this, for each unique path, a vector is created between the SFP. This 3D vector can then be broken down into its 3 constituent angles. While all angles provide information, the angle of interest focused on in this project is the angle which represents the path's direction across the plane perpendicular to the fluid direction, denoted as ( $\theta$ ). This angle was selected due to the channel-like structure within the meniscus, angle  $\theta$  can provide insight into if the effect of fluid direction within these channels.

## Voxel-Connectivity tortuosity

Voxel-connectivity (VC) based tortuosity can be implemented with no prior processing of the data, which is a desirable quality for a simple setup of analysis. All that is required for this method is spatial voxel locations and a set connectivity parameter. The connectivity is directly related to the freedom of movement a path can have, the value can either be set to 6,28 or 26 Figure 2.11a, relating to the connectivity of

voxel faces, edges and vertices respectively [50]. Once these parameters are established, transforming the pore space into a graph is relatively simple, all void voxels are considered nodes and anywhere two void voxels meet the connectivity, an edge is placed, as seen in Figure 2.11b. Due to the high porosity of the meniscus, storing all node and edge data is extremely memory-demanding, this memory requirement, therefore, scales with the connectivity parameter. It was found during this project that graphs with 6 connectivity used up to 8Gb of RAM while 26 connectivity used upwards of 20Gb, this greatly limits the functionality of this method on low-spec PCs. Due to these memory constraints, it was decided that only 6 connectivity graphs were to be used in this project, however, an analysis on the smallest sample was carried out using a high-spec PC (500+Gb RAM) to compare the results between connectivity values and can be seen in Figure(3.5a. As Figure 2.12 demonstrates, the lack of spatial relativity to the centroid of the pore space means paths calculating using this method frequently cut corners or take the 'racing-line' as it were. This is a problematic feature that has been highlighted in other studies [50, 56] has a greater discernible effect as porosity increases, due to the more expansive voids that are ignored.

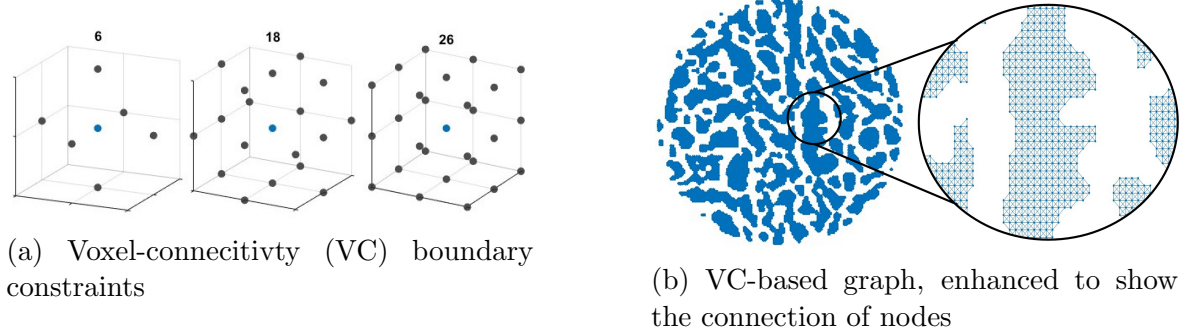


Figure 2.11: Voxel-connectivity tortuosity process

## PNM Tortuosity

Without the volumetric information attached to it, what the PNM in essence represents is a 3D graph of the pore space, with nodes and edges representing the centroids of pore bodies and throats respectively. This representation allows for the utilisation of graph theory functions for pathfinding and tortuosity calculation. While this method and the VC both contain data of the entire pore space, due to the simplifications made during PNM, this graph contains considerably less data, making memory constraints almost non-existent. In addition to this, because the nodes are representative of pore centroids, the available paths will likely be travelling directly through or close to the centre of the pore space. This means that the issue of racing lines will not be an issue.

## Skeletonised Tortuosity

Skeletonised (SKL) is the last method of tortuosity to be considered and is created by introducing a medial-axis transformation to the pore space, identical to that seen in Section 2.2, the name SKL was given to avoid potential confusion with the segmentation

method. As mentioned in Section 2.2, the skeleton represents continuity following the smooth topology of the most expensive regions of the pore space. These expansive regions are also where the least amount of resistance for fluid travelling through the pore space is likely to be encountered, due to the frictional forces at the walls of the channels. Bearing this in mind, it can be assumed that if a stream was to flow through a channel of the meniscus, the skeleton is likely to follow a path not too dissimilar to that of the stream; not taking racing lines or jumping large sections of the simplified pore space, such as in the previous two methods. It is in this way that the SKL method is a sort of 'pseudo-streamline' method, only lacking the essential component of fluid behavioural information solved by solving the Navier-Stokes equations.

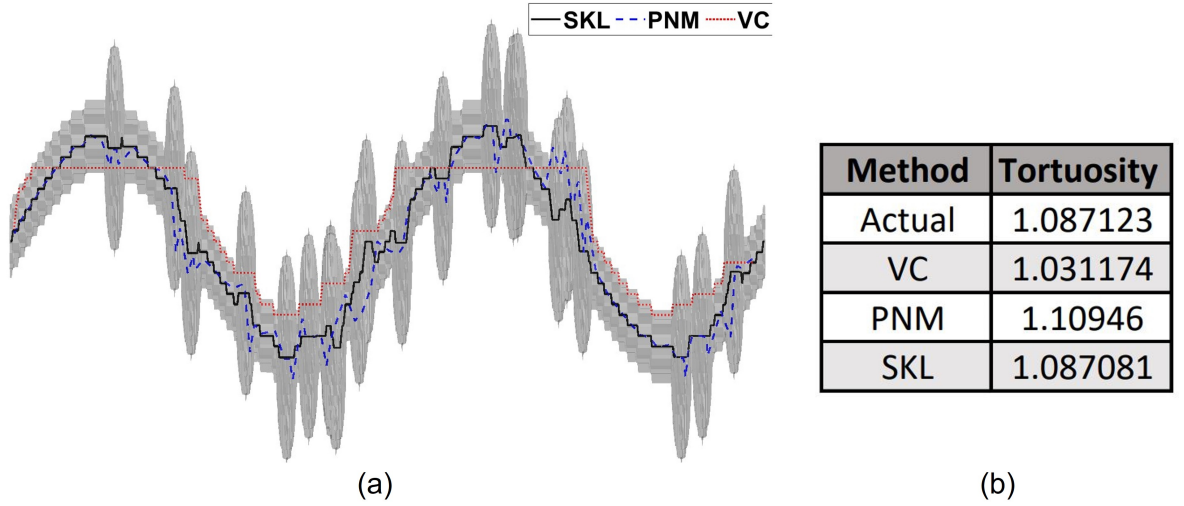


Figure 2.12: (a) Visual demonstration of different tortuosity methods through the same sine wave (b) Table describing the true and calculated tortuosities of the sine wave

## 2.6 Coupling CFD & Image analysis

Before discussing the techniques used to combine CFD simulations with image analysis, a brief overview of the simulations is presented. An edited model of the VOI(3) sample was inserted into Slicer3D, floating points of either material or pore space and notably narrow sections of pore space are removed. This is due to these erroneous regions creating numerical instabilities in the CFD solver. This sample that was manually cleaned of potentially destructive geometry will from hereon be denoted as 'V3E'. The cleaning process was seen to make the largest discrepancy in the connectivity of the pore space, due to the removal of narrow sections which would be characterised as throat during segmentation. While the number of pores and mean pore diameter only fell by 2% & 15% respectively, the number of throats and average coordination number both fell by approximately 50%. While this cleaning process is currently a manual task, the development of this process to be completed through the use of pre-processing within an image editing software such as MATLAB or ImageJ and then converted to a solid model for analysis is in development.

This would be beneficial as it would make the process and results repeatable for others to carry out, but due to technical and time constraints, this was not feasible in the scope of this project. Once cleaned, the V3E sample was input into the CFD software STAR-CCM+ and a series of simulations were carried out, with the boundary conditions of having no-slip walls and an input velocity. This simulation was run with a number of different input velocities ranging from 0.00001-1.6m/s. From these CFD simulations key parameters such as velocity, position and pressure were all extracted. From these simulations, it was also possible to extract fluid 'streamlines', streamlines in this situation refer to the path taken by a particle released from a set start location, calculated by the CFD software. The start locations were chosen using the same methodology set out in Section 2.5, meaning that the streams are all initiated from the most spatially significant regions within the starting plane of the V3E sample (Figure 2.14). All the key parameters mentioned previously were extracted for each streamline.

As the same model is used both in STAR and MATLAB it is possible to analyse the morphological information that STAR cannot calculate. While their coordinate systems differ, STAR using mm and MATLAB using voxels, it is possible to overlap these two models simply by multiplying pixel distance by the resolution of the image to give coordinates in mm and visa versa. The first step was to align the two coordinate systems which was accomplished by creating a new reference origin in the position that correlates in the top left on the start image of the scan. The accuracy of this alignment was checked manually by probing the CFD model at random locations in the model and locating the corresponding point in MATLAB using the coordinates. Once the two models were aligned to a satisfactory degree, which in the case of this project was decided by

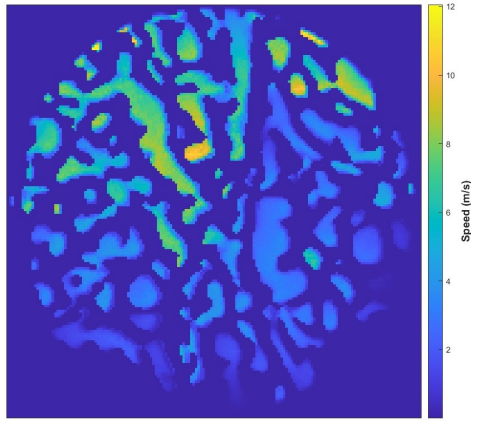


Figure 2.13: Interpolated speed values

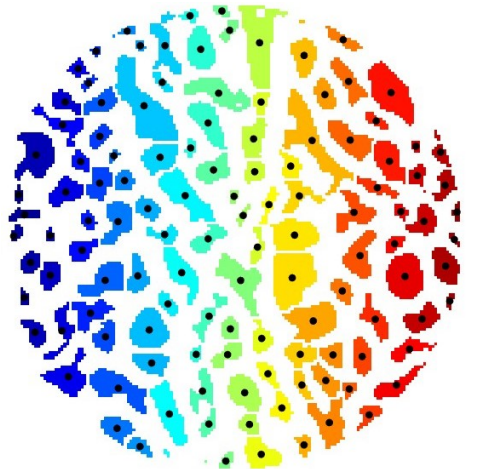


Figure 2.14: Example of segmented pore space

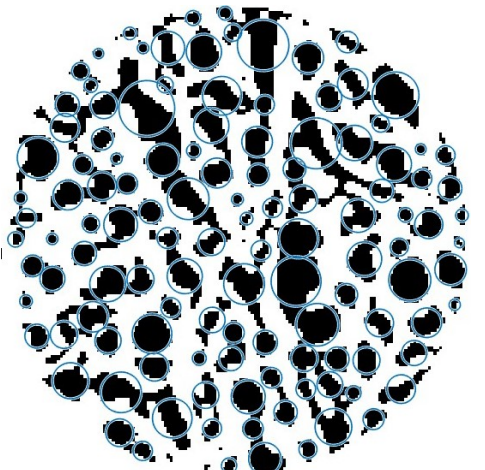


Figure 2.15: Visualisation of equivalent pore diameters

the user assessing the visual agreement of the points, the analysis can commence. The parameters calculated from simulations were tabulated and exported in text format and subsequently imported into MATLAB. As the mesh of the CFD model is much finer than of the voxel resolution in the low-resolution scans, the data must be interpreted at the voxel locations, this was achieved using a gridded-interpolant function built into MATLAB. Once this is complete, any of the key parameters extracted from CFD can be painted into the MATLAB scans (Figure 2.13). From here it is possible to combine fluid flow properties with the morphological analysis conducted in previous sections. As the segmented boundaries between pores are known (Figure 2.14), it is possible to stipulate an equivalent circle with the same area of each pore at every plane along the direction of fluid flow, as shown in Figure 2.15. With these equivalent circles, it is now possible to estimate a value for Reynolds number using the equation 2.6, where  $u$  = fluid velocity (m/s),  $L$  = characteristic length (diameter of the equivalent circle (m)) and  $\nu$  = the kinematic viscosity of water at 37°C ( $7 \times 10^{-6}$ m<sup>2</sup>/s). It is worth noting that the selection of velocity must be taken into consideration, namely, if the maximum value of velocity in the pore should be used, or if the velocities of the entire pore should be averaged and used. To be conservative, this project has utilised the average velocity within the pores. As the data is available in all voxels from this method it is possible to calculate the properties at all pores, even pores that are not included in the streamlines.

$$Re = \frac{uL}{\nu} \quad (2.6)$$

While the information about the entire pore space is now known, this still does not provide information about the fluid direction; for this, streamlines are required. The streamlines provide spatial data of the flow stream as it travels through the pore space. As parameters within the pore space are now known, it is possible to calculate the parameters local to just the streamline. Not only this, but the positional data of the stream can also be viewed as points on a graph, such as that seen in Figure 2.16 which presents plots of the streamlines extracted from the 1.6m/s simulation. This graphing method means it is possible to calculate the hydraulic tortuosity of true fluid streamlines, similar the methods used in Section 2.5.

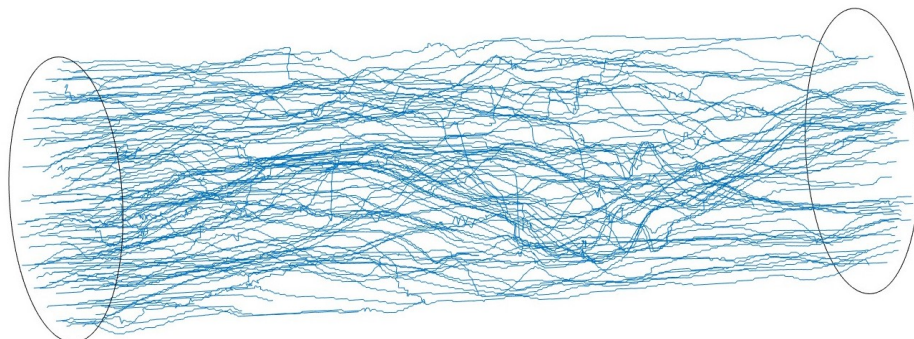


Figure 2.16: Plots of fluid streamlines from CFD simulation

# Chapter 3

## Results

### 3.1 Model validation and performance

As discussed in Chapter 1, there are numerous papers utilising segmentation techniques to characterise the pore space. Only a handful of papers evaluate different methods in tandem [38, 42]. To gauge the agreeability of all the methods tested, an assortment of results have been taken from a collection of papers [35, 38, 41, 42] that characterise the same benchmark datasets [47, 48]. For an overview of all the parameters calculated using the method developed in this project, for these rock samples, please consult Table 5.1 in the appendix.

#### cMBA

The cMBA performance appears to have good agreement with the current literature, with parameters typically ranging between 20-30% error. The exception to this rule is the pore and throat diameters, which see errors on average between 100-200%. This drastic increase in error is due to the discrepancy in how these parameters are defined.[42] defines the pore and throat diameter as the diameter of the ancestor spheres, while this project uses the equivalent diameter of the total equivalent volumetric sphere and surface area respectively, which intuitively will be considerably larger.

#### mMBA

The mMBA performance follows a similar trend to the cMBA, with exceptionally high errors for the pore and throat diameters, for the same reasons explained above. Other parameters (No. Pores, No. Throats and Throat Length) however, all see a 10-20% increase in error, this is likely due to the difference in thinning algorithm used. While both projects use the method set out in [70] as a base, [42] expands on this algorithm as can be seen in the paper, while the MATLAB built-in function also takes inspiration from [74]. The one parameter that sees almost no difference is coordination number which is to be expected as stated in [35].

Sample	Method	No. pores		No. throats		Pore Diameter ( $\mu\text{m}$ )		Throat Diameter ( $\mu\text{m}$ )		Throat Length ( $\mu\text{m}$ )		Coord. Number	
		Reference	Calculated	Reference	Calculated	Reference	Calculated	Reference	Calculated	Reference	Calculated	Reference	Calculated
S1	cMBA	1868	2144	3048	2486	51.18	93.43	24.64	67.91	232.6	156.88	3.26	2.32
	mMBA	1452	1513	2455	2499	65.18	115.31	33	67.49	204.2	206.58	3.38	3.30
S2	cMBA	2021	2582	4942	4464	34.50	62.21	16.26	43.25	154.9	104.16	4.89	3.46
	mMBA	2906	2148	5792	4460	36.10	72.13	19.58	42.07	103.5	113.74	3.99	4.15
S3	cMBA	8926	7008	15105	6551	33.38	68.91	15.02	49.82	161.5	99.68	3.38	1.87
	mMBA	9104	1523	15833	4227	39.84	110.27	20.44	62.00	117	255.32	3.48	5.55
S4	cMBA	9556	7951	13322	7057	33.60	66.20	15.62	48.65	151.1	93.60	2.79	1.78
	mMBA	7199	201	11508	653	41.80	162.79	21.2	91.10	121	481.75	3.2	6.50
S5	cMBA	518	562	1243	857	33.42	68.07	18.98	51.66	187.00	134.35	3.47	3.05
	mMBA	659	477	900	872	35.68	81.15	18.72	50.81	122.50	141.99	3.77	3.66
S6	cMBA	597	610	1234	1041	38	79.72	20.20	59.68	229.20	167.51	4.13	3.41
	mMBA	1022	536	2147	1097	37.58	96.21	19.68	60.24	144.60	175.36	4.20	4.09
S7	cMBA	1016	1351	2741	2553	40.3	70.21	18.60	48.26	187.30	129.92	5.40	3.78
	mMBA	1759	1253	3448	2715	38.02	78.11	20.80	46.56	115.50	131.39	3.92	4.33
S8	cMBA	1324	1656	4209	3980	42.32	78.93	20.94	53.00	194.40	135.17	6.36	4.81
	mMBA	2439	1645	5235	4436	39.64	84.14	22.32	49.23	123.00	133.43	4.29	5.39
C1	cMBA	4576	3276	6921	4325	14.1	33.90	8.04	27.73	88.4	69.05	3.02	2.64
	mMBA	4115	1842	8893	4793	17.32	48.01	9.02	29.01	82.8	98.31	4.32	5.20
C2	cMBA	8508	5828	10336	6584	22.78	51.91	12.34	40.91	122.8	91.91	2.43	2.26
	mMBA	5590	2242	11654	5995	29.24	77.85	14.78	45.76	100.10	165.06	4.14	5.35
Berea	cMBA	6298	7185	12545	9999	30.72	56.54	14.30	40.39	143.7	94.44	3.98	2.78
	mMBA	7611	5533	14328	10324	33.58	67.03	18.18	39.71	99	114.71	3.77	3.73
Estillades	cMBA	2500	2520	-	-	-	-	-	-	-	4.60	3.15	
	mMBA	2612	2130	-	-	-	-	-	-	-	2.60	3.97	
Bentheimer	mMBA	10377	12244	-	-	-	-	-	-	-	3.60	2.74	
	mMBA	18535	16900	-	-	-	-	-	-	-	2.9	3.63	

Table 3.1: MBA validation comparison table  
32

## WA

The WA shows the lowest agreement to its reference results in [33]. while the throat length and average coordination number stayed within reasonable limits (20-25%), the pore and throat diameters are over double this range. The explanation for this is twofold, primarily, the largest distinction between the method seen in the reference paper and the method seen in this project is the mode of smoothing applied. The methodology of this project uses a relatively simplistic median filter with a kernel size of 5 for smoothing the distance map as explained in chapter 2.2. The method utilised in the reference paper is a considerably more thorough series of algorithms that includes: gaussian smoothing, peak identification and finally marker-based watershed segmentation. As one can imagine, this difference in segmentation will lead to a noticeable difference in the pore space characterisation. By inspecting the values in Table 3.2 and cross-referencing with the results seen in Table 3.1, it can be concluded that the pore space characterised using the Watershed segmentation proposed in this project is likely to be under-segmented, explaining the larger pore size and lower coordination number. Secondly, the technique for extracting the throat parameters differs between the projects. While this project utilises the more common method of simplifying the throat geometry to an equivalent circle using the surface area, the reference paper determines an average throat radius by use of distance transform of the 2D projected pore, which is more likely to produce smaller radii proportional to the circularity of the geometry. It is also worth noting that during the analysis of the largest dataset, Bentheimer, it was found that computers with  $\leq 32\text{Gb}$  of RAM could not segment this sample using WA due to memory constraints. While this was eventually accomplished using a high-spec PC (500+Gb RAM), this highlights a computational bottleneck of the algorithm which has not been addressed in current literature.

Sample	Pore Diameter ( $\mu\text{m}$ )		Throat Diameter ( $\mu\text{m}$ )		Throat Length ( $\mu\text{m}$ )		Coord. Number	
	Reference	Calculated	Reference	Calculated	Reference	Calculated	Reference	Calculated
S1	98.36	123.02	49.76	76.67	207.04	224.02	2.64	2.07
S2	61.28	84.04	32.44	49.31	120.13	135.37	3.80	3.81
S3	65.10	85.21	28.52	51.27	143.84	150.09	2.49	1.13
S4	65.36	81.93	30.98	48.97	133.83	143.06	2.07	1.04
S5	52.14	95.18	43.70	70.03	128.81	161.98	2.45	3.20
S6	66.66	119.70	53.46	87.79	145.57	201.53	3.23	3.64
S7	70.22	98.99	37.90	58.19	138.38	158.89	4.11	4.37
S8	54.32	103.52	42.48	62.90	126.60	153.34	3.56	5.45
C1	22.78	48.07	23.98	39.75	62.49	88.34	2.12	2.72
C2	36.00	66.82	30.20	55.39	94.29	127.09	1.55	1.83
Berea	52.44	76.97	29.40	47.37	112.98	133.56	2.90	2.65

Table 3.2: WA validation comparison table

## Tortuosity

The results shown in Table 3.3 represent the tortuosity using the VC-based tortuosity method or 'DSPSM' as it is denoted in [50], following the method described in the paper. This is relevant as this method differs from the method described in 2.5 but has been incorporated here for the use of validation. It would have been desirable to also evaluate the skeletonised or 'SSPSM' tortuosity, however, due to ambiguity in the paper of how the start and finish points were selected and given that both the methods work on a similar methodology, it was decided to exclude this method from the validation process. The results show very good agreement, with the error between results ranging between 5-15%. The overestimation in tortuosity could be explained if the reference paper performed any pre-filtering of the image that was not included in the report or if there is the removal of results that appear to be outliers.

Sample	Tortuosity	
	Reference	Calculated
8% Porosity	1.91	2.13
10% Porosity	1.76	1.99
13% Porosity	1.57	1.69
15% Porosity	1.46	1.63
17% Porosity	1.4	1.47

Table 3.3: Tortuosity validation table

## Computation time

With analyses such as these, minimising computation time is commonly a primary objective. As described in Chapter 2 there is often an equilibrium that must be met between information retention and computation time. Figure 3.1a clearly demonstrates the vastly superior computation time of the WA, followed by the mMBA and lastly the cMBA, all speeds were calculated using a Dell Latitude E5570 (16Gb RAM, Intel(R) Core(TM) i7-6820HQ CPU @ 2.7 GHz Processor). It is also worth noting, that as discussed in Chapter 2, the WA does not require any usage of parallel computing, while parallel computing has been used during the MBA methods during the creation of the MIS into the label matrix. While this is not strictly necessary, the implications of not utilising this ability greatly increase computation time. There have been proposed methods around this computationally demanding section of the MBA Figure 3.1b, [38] and [42] both incorporate progressive region-growing algorithms, by painting isolated voxels, corresponding sphere locations and iteratively expanding these until all possible void voxels are contained. While neither of these studies explicitly expresses the difference in performance between sphere creation and region-growing methods, it can

intuitively be seen that the difference in these methods could contribute to a difference in pore and throat geometry as interfaces will vary depending on the method selected.

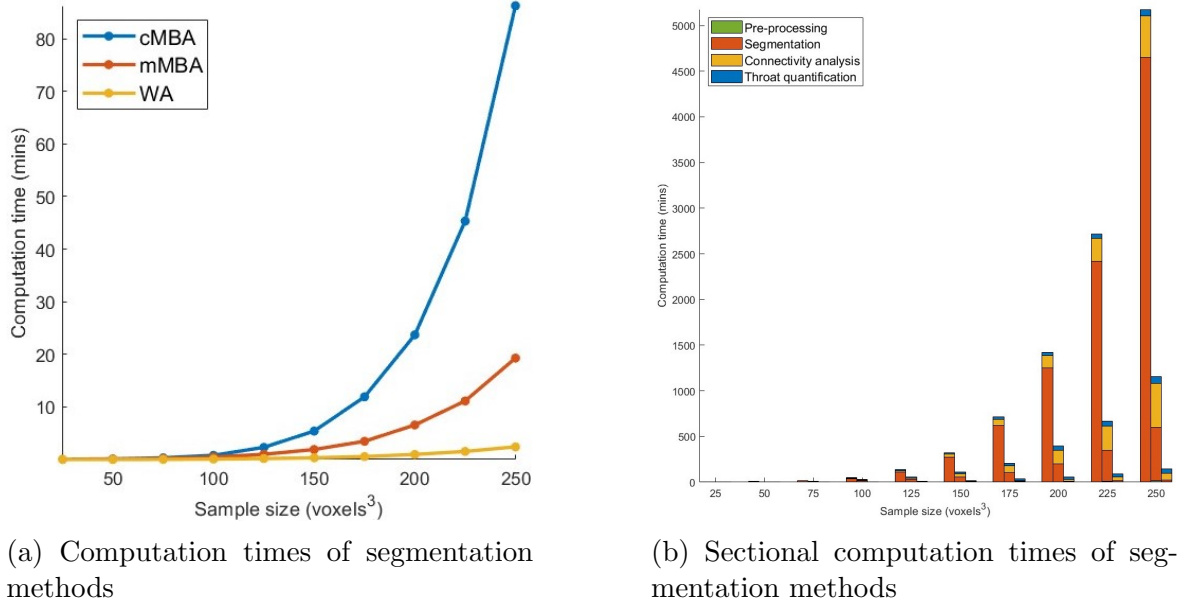


Figure 3.1: Computational time comparison of segmentation methods

## 3.2 Characterisation of pore space

With the performance of the segmentation method explored on benchmark datasets, it was then acceptable to characterise the pore space of the samples of this project. This section will cover the primary parameters that have previously been explored in Chapter 2 and Section 3.1. Comparisons will be made between the different segmentation methods along with some additional factors that have not previously been discussed. Table 3.4 contains a brief overview of the results of the primary parameters calculated from the different segmentation methods. All the figures below pertaining to comparisons of the segmentation models, unless stated otherwise, present the mean values of the normalised results from all 4 of the meniscus datasets. To see the individual results please consult Figures 5.1 onward in the appendix.

Sample	Resolution ( $\mu\text{m}$ )	Porosity (%)	Method	No. Pores	No. Throats	Avg. Pore Diameter ( $\mu\text{m}$ )	Avg. Throat Diameter ( $\mu\text{m}$ )	Avg. Throat Length ( $\mu\text{m}$ )	Avg. Connections			Tortuosity		
									VC	SKL	PNM	VC	SKL	PNM
VOI(1)	6.25	59.6	cMBA	11294	42171	73.78	48.76	119.38	7.47					
			mMBA	11801	54437	75.37	44.50	118.36	9.23	1.44	1.64	1.11		
			WA	5273	24554	111.35	63.61	159.07	9.31					
VOI(2)	6.25	61	cMBA	7883	29627	81.65	53.98	139.18	7.52					
			mMBA	8435	38440	82.07	49.05	137.33	9.11	1.43	1.64	1.11		
			WA	4216	20091	121.94	69.91	170.65	9.53					
VOI(3)	6.25	62.7	cMBA	2059	8113	80.64	51.96	125.98	7.88					
			mMBA	2253	10577	80.97	47.47	121.47	9.39	1.42	1.63	1.10		
			WA	1017	4946	118.10	66.40	163.55	9.73					
VOI(4)	6.25	58.6	cMBA	10536	44899	85.35	55.90	137.43	8.52					
			mMBA	11415	55769	83.50	50.15	134.13	9.77	1.43	1.67	1.10		
			WA	6103	32775	122.84	71.43	165.03	10.74					

Table 3.4: Meniscus samples properties

## Pore-size

As the pores make up the majority of the pore space it is important to carefully interpret the results of the pore-size distributions (PSD). Figure 3.2 shows the effect of each segmentation method on the PD. while we can derive from Table 3.4 which of the models produces the largest pores on average, the PSD provides additional information that can provide insight into the nuances of these models. For instance, despite the average pore sizes of the cMBA and mMBA being very close, their distributions are considerably different. The mMBA is seen to create pores that are more uniformly sized, this can be identified from the standard deviation of the mMBA being lower around the average. This is likely the result of the MA not branching into regions that fit the criteria to be classified as pores but the criteria of branching in the MA algorithm.

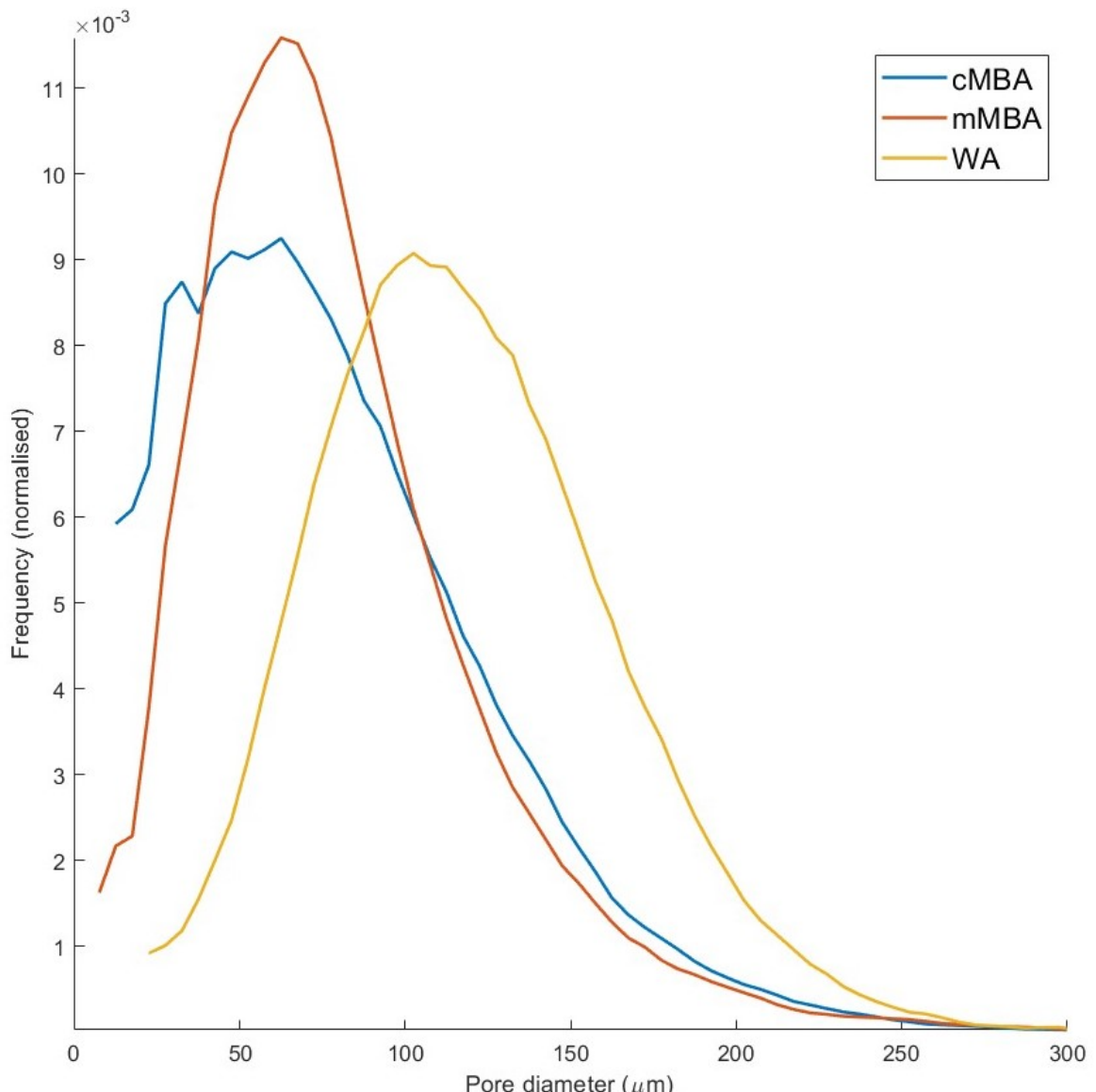


Figure 3.2: Pore-size distribution comparison of segmentation methods

## Connectivity

Reassuringly, the average coordination number between models stays relatively constant between models. There is a clear correlation between all models relating to the average pore diameter and the coordination number, this is an expected relationship as a larger diameter corresponds to more voxels contained within that pore and hence, the higher the probability of these voxels connecting with voxels of other pores. Contradictory to this, however, despite the mean pore diameter of the cMBA and mMBA being very close, the average coordination number differs considerably. This can be explained using the PSD, the cMBA contains a significantly higher number of small pores (diameter $\leq 50\mu\text{m}$ ), these smaller pores break up the continuity of larger pores which prevents them from achieving the higher coordination number seen in the mMBA. This further perpetuates the importance of reviewing the parameter distributions to interpret the models. It is also worth noting that the mMBA also experiences the least amount of variation between samples, meaning that it is the most consistent model to use in terms of consistency.

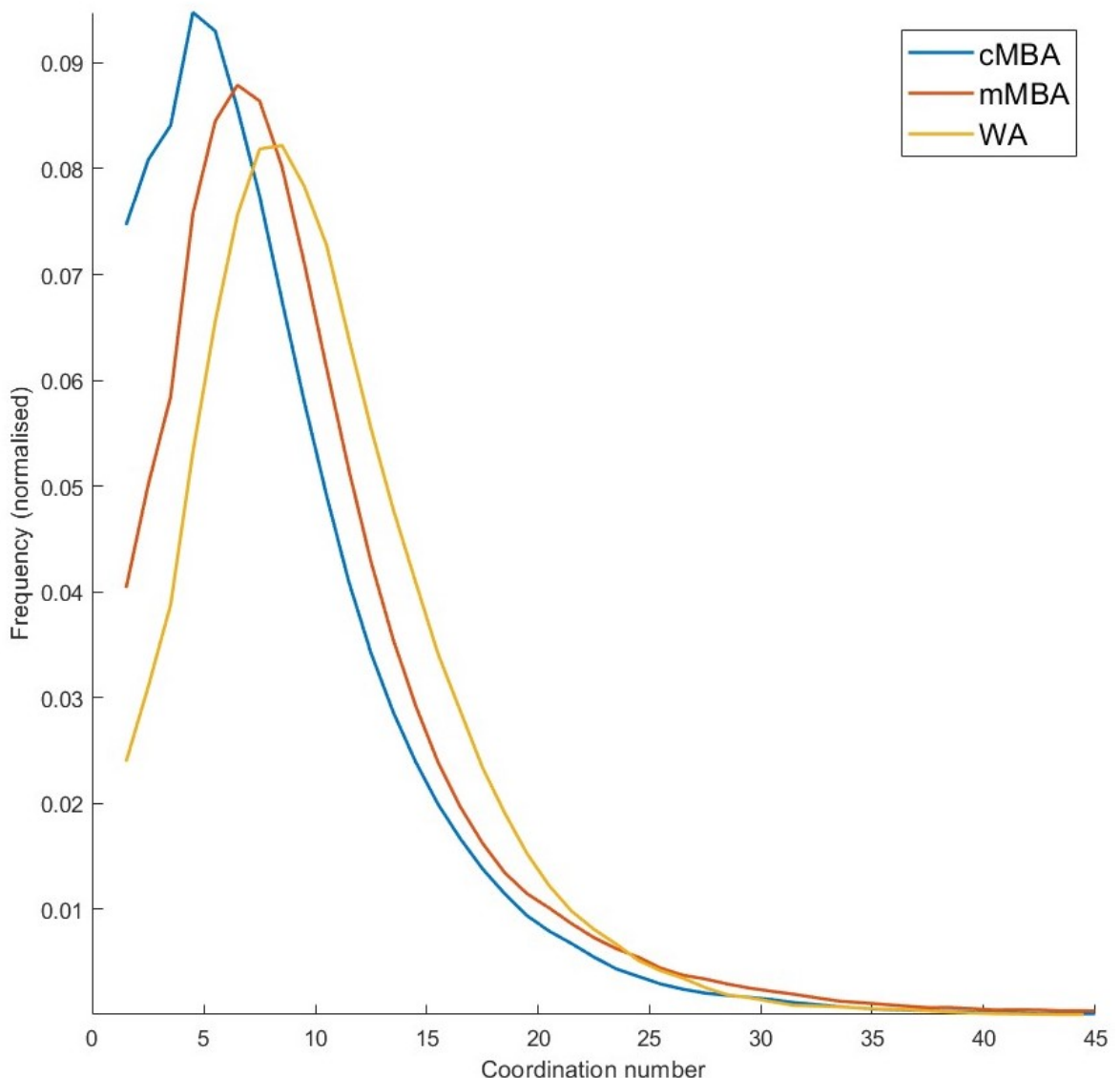


Figure 3.3: Connectivity distribution comparison of segmentation methods

## Throat properties

The throat diameter distribution is similarly comparable to that of the PSD, with the mMBA and cMBA following very closely to one another but the mMBA presenting a more uniform distribution. The WA is seen to produce larger throat diameters, this is to be expected as the larger pores produced in the PSD will have greater connected surface areas to one another. The length of the throats also replicates this trend. Unsurprisingly, the length of throats from the WA are longer as a result of the pore centroid from the larger pores being further apart.

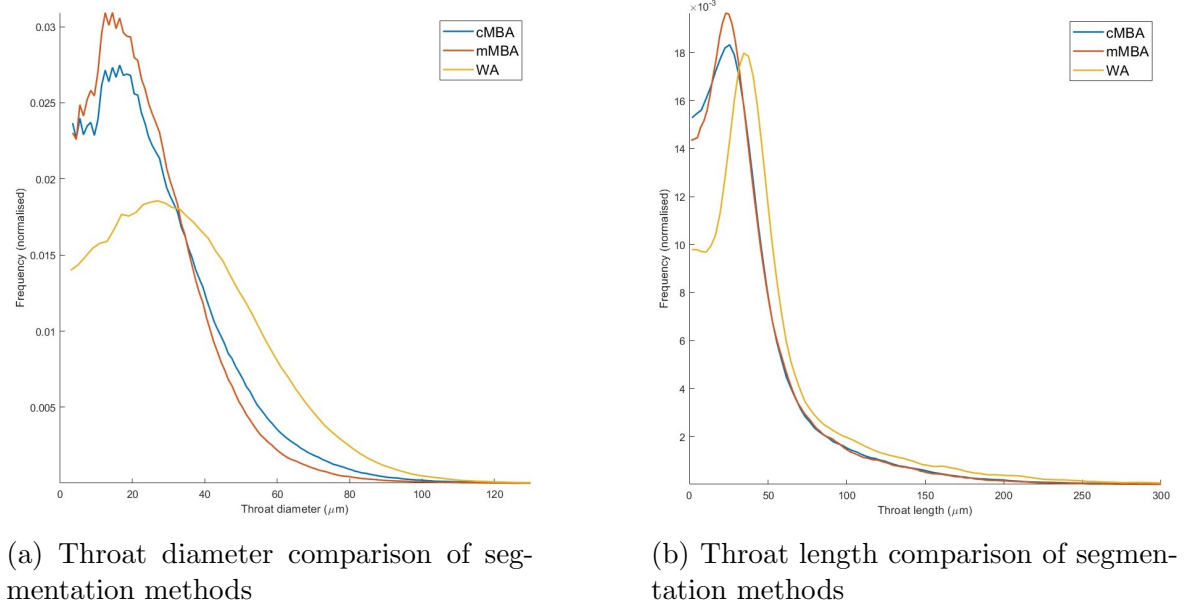
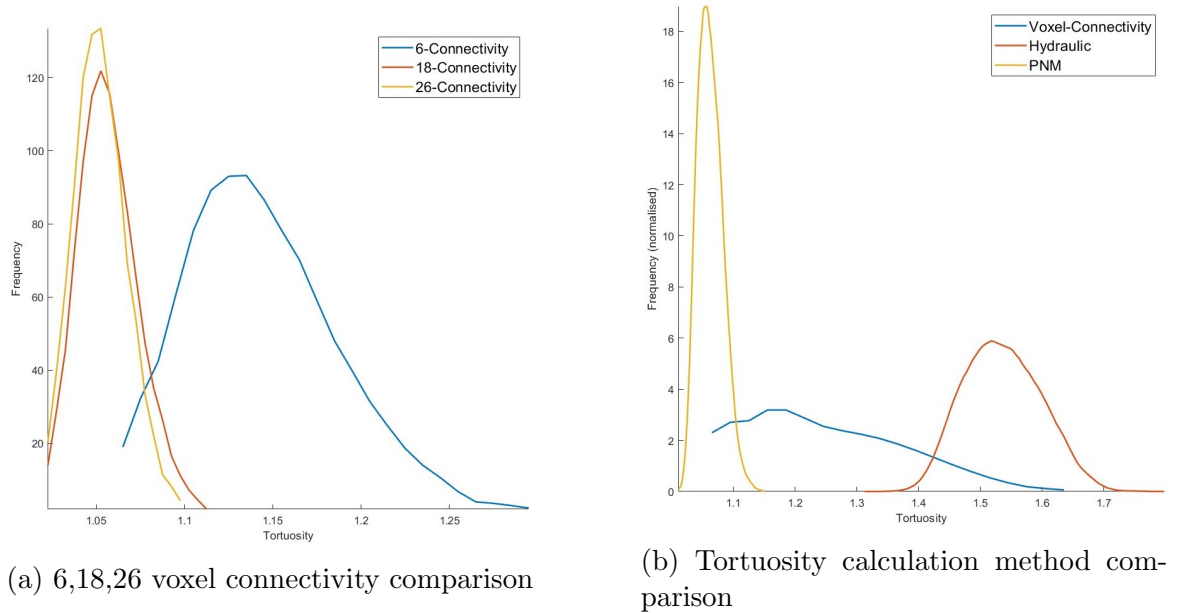


Figure 3.4: Throat parameter comparisons of segmentation methods

## 3.3 Tortuosity

As discussed in Section 2.5, Table 3.4 shows the characteristic tortuosity of using the three different methodologies, there is much more to learn from this data, however. Firstly, as mentioned in Section 2.5, one of the limitations of the methodology proposed in [50] is that the voxel connectivity is limited to just 6, with no further investigation being carried out. This project has expanded upon this, Figure 3.5ba presents the distribution of tortuosities for the same paths, each done with the three voxel connectivities. Sample VOI(3) was selected as it is the smallest of the datasets and only the Z-direction has been interpreted. It is clear to see that the discrepancy between using a 6 voxel connectivity vs the 18 or 26 is exceptionally large, demonstrating that giving the path the ability to travel across voxel edges drastically reduces the necessary path length. This is unsurprising as if a path must change direction in a non-orthogonal orientation, then the 6 connectivity path will be forced to create a path that is very 'snaking'. For the 6 connectivity to change direction it will be either 1.4 or 1.7 times more than using one of the higher connectivities.

Secondly, 3.5bb shows the diversity in results of the different methods of calculating tortuosity. What is interesting about this plot is the vast disparity between the SKL and the PNM methods. Despite both of these methods travelling through the centroid of the void space, the PNM tortuosity is vastly lower than the SKL. This is due to the considerable reduction in complexity of the pore performed during PNM. All topological information between pores is lost, greatly reducing path length as the path is simply traversing a straight line. It can be theorised that a more segmented pore space will likely lead to a result closer to that of the SKL, but remaining smaller. The segmentation method used for the calculation of tortuosity using PNM methods shown in this section was cBMA as this performs the most accurately to current literature.



Lastly, it is important to quantify how anisotropic the meniscus medium is. As previously stated, the tortuosity shown in Table 3.4 is the characteristic tortuosity [58], but the orthogonal components of this characteristic value are also of great value. What Figure 3.6a and Table 3.7 demonstrates is that the meniscus is almost bidirectionally isotropic in the X & Y directions. In addition to this, the tortuosity in the Z-direction is distinctly lower than its perpendicular counterparts. This demonstrates, statistically, that there is a preferential direction within the meniscus that provides less topological resistance to movement through the medium. The characteristic tortuosity ( $\tau_c$ ) and degree of anisotropy ( $\sigma$ ) are variable both derived from [58] and are calculated using the equations below:

$$\tau_c = 3[\tau_x^{-1} + \tau_y^{-1} + \tau_z^{-1}]^{-1} \quad (3.1)$$

$$\sigma = \frac{\max(\tau) - \min(\tau)}{\tau_c} \quad (3.2)$$

This anisotropy is in fact twofold, as there is additionally a preferential direction within the Z-direction. Using the methodology for calculating path orientation set out in section 2.5, every path has an associated orientation in the XY plane, describing the 2D trajectory of the path across the sample. These orientation angles have been rounded to their nearest integer value and grouped together. The average tortuosity of these groups has then been calculated for each associated group. These results have been displayed in the polar plot in Figure 3.6b. The polar plot clearly presents a preferential orientation within the range of 270-330°.

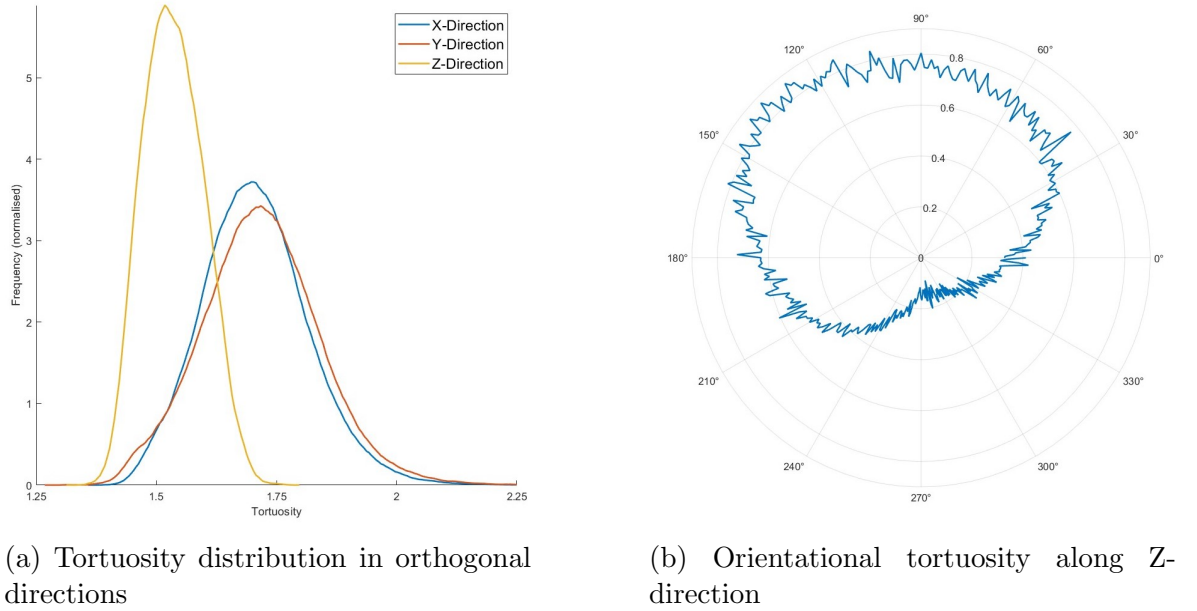


Figure 3.6: Twofold anisotropy in meniscus samples

Sample	Model	Tortuosity ( $\tau$ )				Anisotropy ( $\sigma$ )
		$\tau_x$	$\tau_y$	$\tau_z$	$\tau_c$	
VOI(1)	VC	1.53	1.53	1.29	1.44	0.17
	SKL	1.72	1.70	1.52	1.64	0.12
	PNM	1.14	1.13	1.06	1.11	0.07
VOI(2)	VC	1.51	1.52	1.29	1.43	0.17
	SKL	1.68	1.71	1.55	1.64	0.10
	PNM	1.13	1.14	1.07	1.11	0.06
VOI(3)	VC	1.52	1.53	1.30	1.42	0.16
	SKL	1.72	1.72	1.50	1.63	0.13
	PNM	1.13	1.13	1.05	1.10	0.07
VOI(4)	VC	1.52	1.52	1.29	1.43	0.16
	SKL	1.73	1.76	1.55	1.67	0.12
	PNM	1.12	1.12	1.06	1.10	0.05

Figure 3.7: Tortuosity characteristics of meniscus samples

### 3.4 Solid-body Modelling

As discussed in Chapter 2 the potential issues with solid-body modelling are the prevalence of impossible geometry or overlapping pores after the geometrical simplifications have been applied. The adapted pore network modelling algorithm described in Section 2.4 eliminates the possibility of impossible geometry, it cannot fully prevent the overlapping of pore spheres. To evaluate the potential severity of these effects, after the simplifications have been applied all pore spheres are investigated to detect any collisions between pores that do not possess a connection in the true pore space. The results of this investigation can be seen in Table 3.5, with the % of sphere collisions referring to the ratio of how many pores contain these unrealistic connections relative to the total number of pores in the model. The results demonstrate that in all samples, unrealistic connections occur that are non-existent in the true pore space, this poses significant questions to the validity of these solid models. Additionally, it is apparent that the mMBA created models with the lowest number of these unrealistic connections, being 60% lower on average relative to the other segmentation methods. The process and subsequent final result of the solid-body modelling process can be seen in Figure 3.8 & 3.8c respectively.

Sample	Model	Sphere Collisions (%)
VOI(1)	cMBA	9.43
	mMBA	3.12
	WA	9.29
VOI(2)	cMBA	9.3
	mMBA	3.37
	WA	11.79
VOI(3)	cMBA	8.06
	mMBA	2.66
	WA	35.34
VOI(4)	cMBA	8.91
	mMBA	3.17
	WA	10.83

Table 3.5: Pore sphere collision of solid-bodies

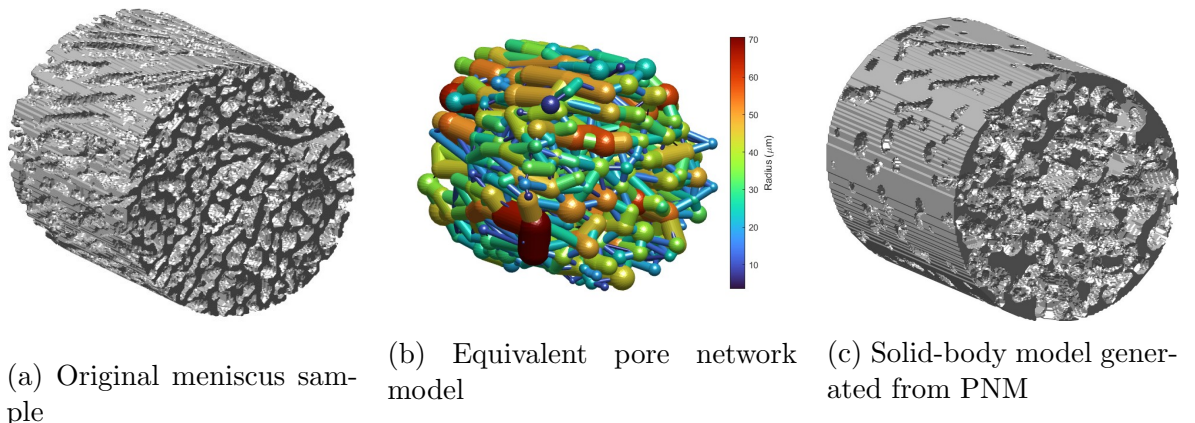


Figure 3.8: Solid-body modelling process

### 3.5 Determination of fluid properties

From the methodology set out in section 2.6, it is not only possible to discover additional properties of the streamlines simulated, but of the entire pore space. Each streamline can be tacked to reveal the full geometry with which the fluid is flowing through, an example of which can be seen in Figure 3.9 (top); the colourmap of which is represented in the plot below in Figure 3.9 (middle). The ability to determine fluid properties through the entire space allows for the additional calculation of average values of properties along the entire sample plane at each Z-step iteration, which can be seen in Figure 3.9 (bottom). The property evaluated in Figure 3.9,  $Re$ , presents a clear distinction between the global and local values, with the local at certain intervals being 2-3 times higher than that of the global. Additionally, while the  $Re$  calculated does not inherently reach values  $\geq 2000$ , by comparing the calculated channel diameters with the range of mean channel speeds observed, it was found that turbulent flow was possible in 83 locations. If instead the maximum channel speed is taken rather than the average, this number escalates to 12000.

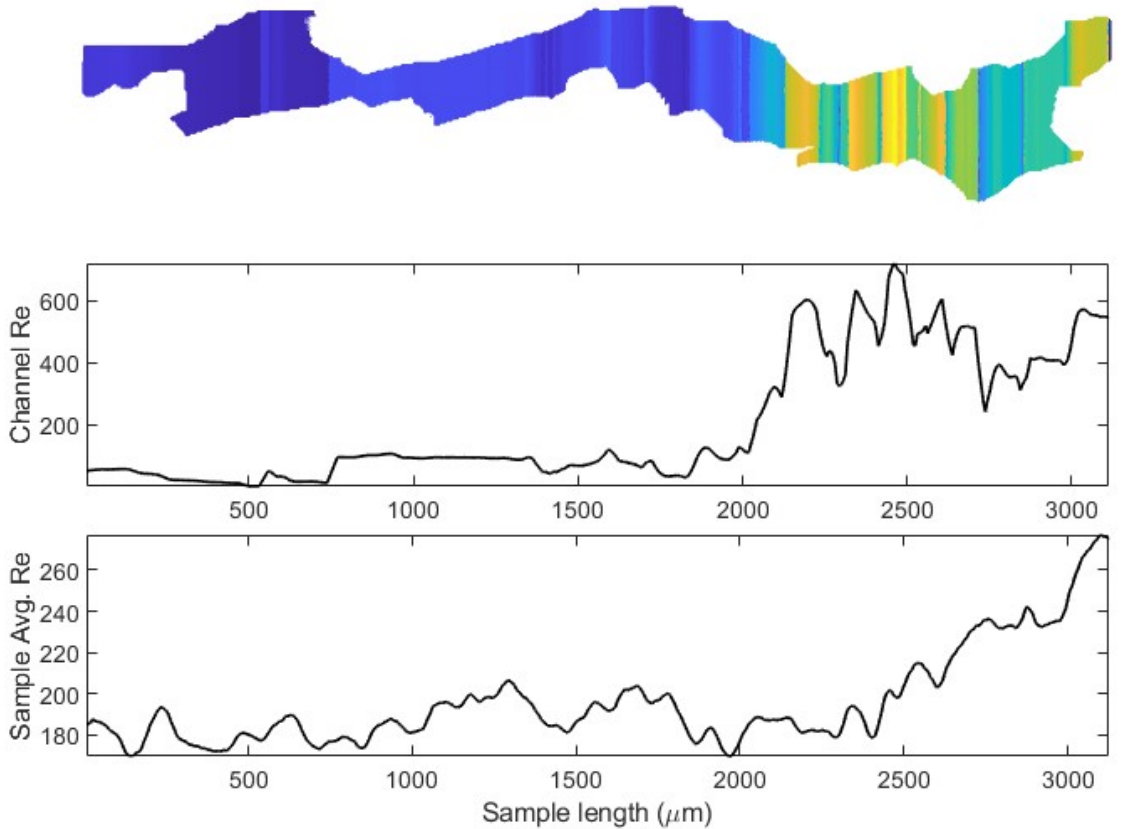


Figure 3.9: Comparison between global and local  $Re$

The tortuosity of the streamlines has been calculated to yield the true fluid tortuosity fields within the meniscus. There are multiple key points to take from this data, but before this, only streams that terminate in the top 10% of the sample are considered, this is to remove paths may contain erroneous values due to stagnation or premature termination and to match the path taken by geometric tortuosities that also abide by this condition. Firstly, Figure 3.10a, demonstrates the variance in hydraulic tortuosity

with inlet velocities, 0.1mm/s have lower tortuosities and 1.6m/s. Secondly, a comparison of the geometric tortuosities with the hydraulic tortuosity for the V3E sample can be seen in Figure 3.10b, with the hydraulic tortuosity falling in between the SKL and VC. Finally, it is apparent to see in Figure 3.10c that the SKL and hydraulic tortuosity both share the same preferential orientation. This reinforces that the channels are arranged in such a way that provides less resistance to fluid moving through the medium and the geometric tortuosity can be used to predict true fluid properties of the meniscus.

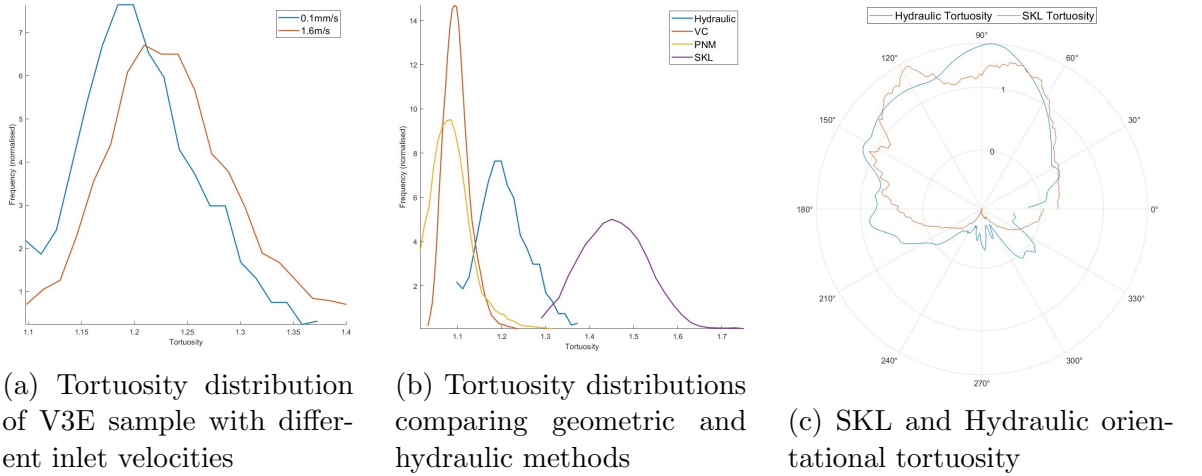


Figure 3.10: cfd tort

Understanding what parameters most influence the fluid path is invaluable to better improve our understanding of the medium itself. To do this, the parameters of every streamline have been captured at every Z-step along the fluid direction, these values have then been averaged out for the entire stream to provide a broad overview of the characteristic of each stream. The characteristic values have then individually compared against each other to return a pairwise linear correlation coefficient using the 'corr' function built into MATLAB. These correlation coefficients can then be plotted as equivalent  $R^2$  values, the final result being the large correlation plot seen in Figure 3.11. This plot can be used to infer relationships between structural, morphological and topological parameters with fluid properties of streams.

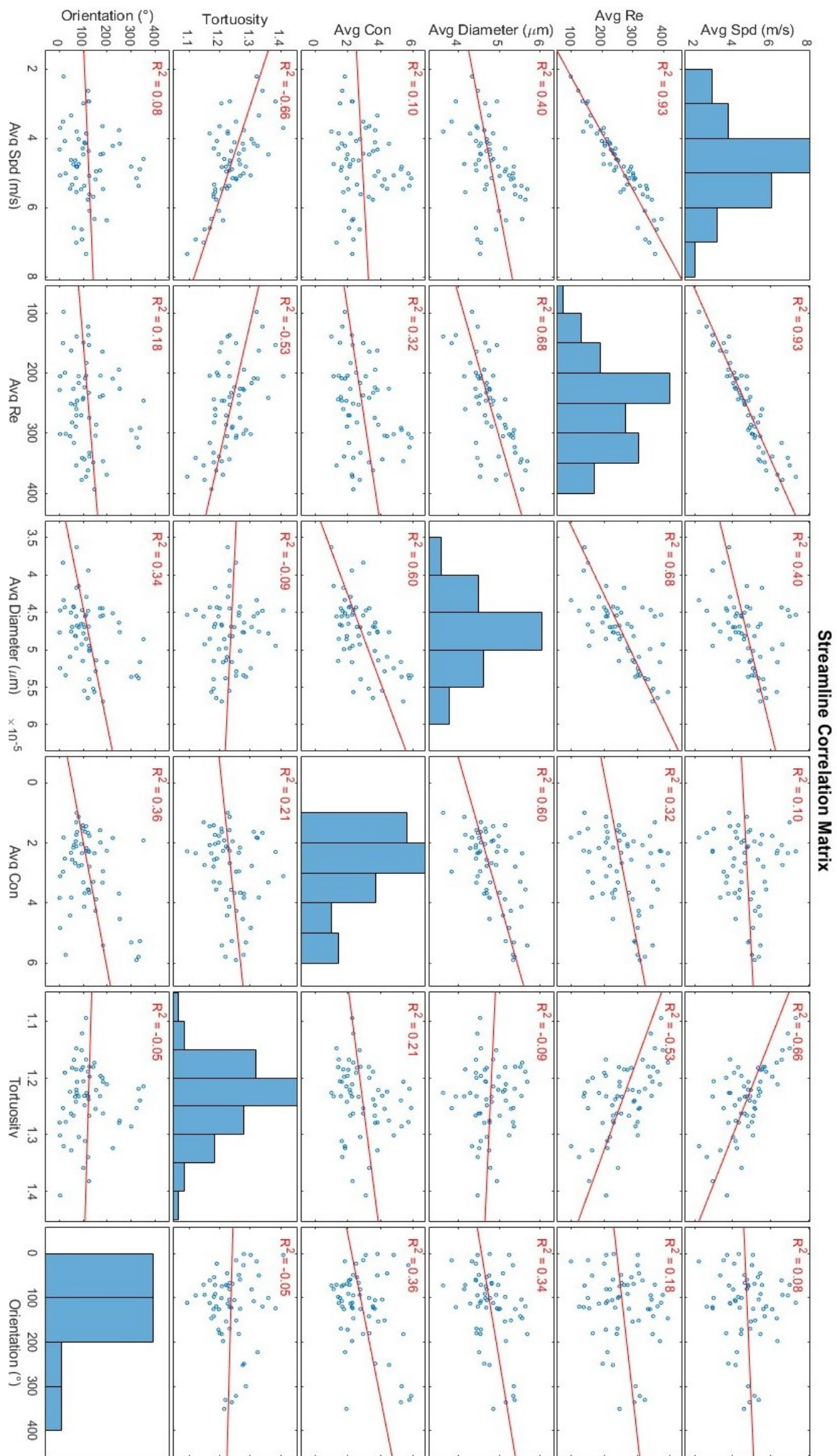


Figure 3.11: Structural parameters correlation plot  
45

# **Chapter 4**

## **Discussion**

### **Characterisation of soft tissues**

The suitability of using utilising PNM of fibrous, high-porosity media and biological materials is still a new concept and thus, research is underdeveloped. This study has evaluated the segmentation and subsequent characterisation of complex, heterogenous, soft tissue samples using a trio of the most popular methods. The results of which, do not define a clear-cut choice for future selection in characterisation. If viewing the analysis through the lens of agreeability with existing literature, then the cMBA is the most suitable choice, the fact that this method has been used for the longest duration means that there is a plethora of trustworthy experiments and evaluations using this model. However, out of all the methods used, the cMBA had the worst scaling between computation time and sample size. This drawback could be detrimental in areas with frequently high-porosities or where samples are extracted from multiple regions to be analysed. Which, due to the heterogeneous nature of menisci and biological tissues in a broader sense, would be in tissue modelling. For this method to be truly viable, efforts must be put into developing ways to reduce the segmentation portion of the PNE process. Studies such as [38, 42] have developed tools to reduce the time of this process by using region-growing algorithms, however, investigations into how the use of these algorithms affects results and their effectiveness are currently non-existent. Other methods have been produced to reduce the computation of the cMBA function by minimising the number of necessary calculations, such as the mMBA. The mMBA did agree reasonably well with the existing literature, however, this is difficult to gauge to the lack of uniformity on how the MA is derived. The two reference papers chosen for comparison in this project [41, 42] each adopt a different algorithm for constructing and weighting the MA. Unsurprisingly, this makes the selection and validation of the results an arduous process. Therefore, the current literature would likely benefit from an explorative study investigating which MA algorithms are best suited for a variety of materials. Aside from this, the mMBA boasts some significant advantages over its more agreeable counterpart. Most notably, the mMBA scales much more favourably with increasing sample size, cutting computation time down by 60-75% in larger datasets. In addition to this, the parameter distributions show us that properties derived using

mMBA are more uniform. This is a desirable trait to possess as if we can reliably predict that a value will fall between a narrower range, then fewer errors are likely to occur when generating datasets or manufacturing models. It is likely this uniformity of properties is what contributed to the solid-body models of the mMBA having the lowest percentage of pore-body collisions out of all the segmentation methods, this can intuitively be expected as if pore-sizes are distributed more evenly across the sample after size reduction fewer are less likely to be in contact. The final method that has been evaluated for the investigation of this project was the WA, while this method is still the most modern of the method tested, it has been shown to have great success in recent studies [33, 66]. This method decimates the competition in terms of computation time, with large samples taking under 10% of the time that the sample would take for the cMBA to analyse a sample at the same. This speed, however, does come at the cost of stability. The WA is highly susceptible to over-segmentation, which is often remedied using image filtration techniques, these techniques however are frequently not described comprehensively in the literature. To obtain comparable results, future research must unambiguously disclose all pre-processing and filtering techniques utilised and ideally, provide some level of investigation of what the expected outcomes are if these protocols are not followed. This project has broached this issue by evaluating various thresholding and filtering techniques. The most notable of these tests highlighted the importance of filtering on the distance map before segmentation. The distance map was segmented using a median and gaussian filter, following the works of [37] and [36] respectively. The gaussian filter was shown to segment the pore space  $10\times$  more than that of the median filter, presenting the importance of local maxima removal or merging [36, 75]. Ultimately, median filtering was chosen due to more support work in the literature and limitations of MATLAB marker-based watershed segmentation. After comparing results with those from existing literature, however, it was found that the watershed model was in fact under-segmenting the pore space, consistently producing the largest pores, throats and coordination values. This was likely due to a difference in pre-processing techniques which as stated, is what makes troubleshooting this method more difficult. The WA was also seen to create a computational bottleneck during the segmentation process, with computers having  $\leq 32\text{Gb}$  RAM being unable to segment the Bentheimer sample due to memory constraints.

To answer **RQ1**, the final consensus of this project is that yes, PNM is suitable for modelling high-porosity biological media. Current research has show success in fibrous[36, 76], hierarchical[77] and artificial[46] samples. This consensus comes with the caveat that further work needs to be done on adapting these methods for higher porosity materials, improving standards on the dissemination of what procedures have been employed and providing better analysis of the outcomes when processes are ignored. To elaborate upon this consensus whilst addressing **RQ2**, the decision of which segmentation method to employ should be carefully thought out and dependant on the desired scope and goals of the need. If high volumes of data are to be analysed

with a moderate tolerance acceptance, then the WA is the choice pick. If accuracy and reliability are the most valued aspects of the analysis then the tried and tested cMBA would be better suited. If the objective is solid-body modelling and better uniformity of results is desirable, mMBA has been demonstrated to be the best method for this. Additional caution should be taken if the material is being characterised for the desired end product of having a solid-body model of the simplified pore space for use in manufacturing or the modelling of physical phenomena. Even after implementing a bespoke pore reduction algorithm to minimise the number of destructive geometries, all models in every sample were still shown to contain overlapping pores which in the real structure are not actually connected. These overlaps will of course misrepresent the pore space and have an effect on fluid properties through the medium or mechanical response if loading. It is also worth noting, that while some of the simplification choices are made to preserve macroscopic parameters such as porosity [37], in practice when these simplified models are constructed, porosity was found to be 5-15% higher on average. This is due to the necessary increase in pore diameter to match that of constituent throats and the volume of space taken when creating the throats.

## Topological analysis of the meniscus

As discussed in chapter 1, while tortuosity is regarded as a highly influential parameter in the characterisation of the pore space, there is a surprising lack of standards when it comes to terminology and definitions [53]. This ambiguity leads to confusion about what the true tortuosity of a medium is and how it should be determined. To help answer these questions, this project has evaluated three different methods of analysing tortuosity: Voxel-connectivity (VC), pore network modelling (PNM) & skeletonised (SKL). VC tortuosity is simple to set up and calculate, however, requires a copious amount of computer memory to utilise effectively or at all. This memory usage is impacted by three parameters: sample size, porosity and voxel connectivity. High porosity is unavoidable in this analysis and while sample size can be adjusted technically speaking, this is not desirable and leads to a loss of information and continuity of the pore space. The connectivity between voxels is in fact a controllable parameter and has been restricted to a value of 6 during this project, for the reason of saving time and making these results more accessible for repeating. A brief investigation into the effect of using higher connectivities demonstrated that increasing the connectivity from 6 to 18 significantly reduced the range of tortuosities and in fact made the results more uniform. The reduction in tortuosity from increasing the connectivity from 18 to 26 was relatively minor, therefore, it is suggested if there is a requirement to obtain the tortuosity using a comprehensive connectivity value, it is suggested to only use 18 to save on memory consumption. The VC method spanned the largest range of all the methods, with the average falling between the PNM and SKL. This method could potentially have value as an initial approximation of the potential limits of tortuosity in the medium, which is assisted by its simple set-up and lack of pre-processing re-

quired. The PNM method is figuratively the inverse of the VC, rather than include all information about the pore space it uses only the minimum. This method incorporates the topology of the simplified pore network and therefore can be easily introduced as a section of the PNE process. As this method is the inverse of the VC, so are its characteristics. As only the simplified pore space is considered the memory usage of this method is almost negligible. This simple model, naturally, has the drawback of being over-simplistic. With such little information about the topology of the pore space, the straight paths between pores neglect the majority of the details that make the pore space difficult to traverse. Due to this, the tortuosities found using this method are very low, despite following paths that are located through the centre of the pore space. Considering these drawbacks, it is not recommended to use this method when trying to predict physical phenomena through the pore space, for instance, hydraulic properties or diffusivity. That does not mean that this method is without use however, thanks to its low memory use memory usage this method is ideal for finding a high quantity of paths rapidly. This method is also well suited for large datasets when creating graphs as using the VC or SKL method can be too memory intensive or slow to calculate. It is also possible to find more elaborate details about the pore space using PNM, for instance, the results shown in Figures 3.6 & 3.10c conveying a preferential orientation in the fluid direction can just as easily be found using the PNM method. The final method evaluated the skeletonised pore space or SKL method. This method is arguably the most topologically informed of the methods, taking all the information provided by the pore space, similar to the VC method, and condensing it to the most topologically significant space (the centroid of the pores), similar to the PNM. This method can be viewed as a 'best of both worlds' approach, with significantly lower memory requirements than the VC but retaining enough critical information to provide far more accurate paths than the PNM. It is this strict requirement of smoothly following the winding topology of the meniscus that means this method produces the largest of the tortuosities. Being the most spatially informed method, the SKL could be viewed as representative of the true potential topological resistance a fluid streamline would encounter while travelling through a medium; it is then only natural to assume that this method would most accurately reflect the hydraulic tortuosity found in CFD experiments. To address **RQ4**, when plotted together in Figure 3.10b, it was found that the hydraulic tortuosity actually fell between the SKL and VC tortuosity. This is similar to the results seen in [50] (Figure 14), where the relationship between hydraulic and SKL tortuosity is seen to diverge as porosity increases. Considering the porosities evaluated in this project are  $2\times$  that investigated in [50], it is unsurprising that this distinction is so large.

Despite which method is used, all of these tortuosity methods can be used to quantify anisotropy in media. By calculating tortuosity in all orthogonal directions, it has been found that, in regards to tortuosity, all the menisci samples were virtually isotropic in the X & Y direction, while the Z-direction raises noticeably less topological resistance.

This, in theory, could demonstrate that the meniscus is grown in a way that to possesses a more permeable direction. What this anisotropic structure contributes to the function of the meniscus is still unknown, but discovering it exists and quantifying it is the first step in finding out. The characteristic tortuosity ( $\tau_c$ ) and measure of anisotropy ( $\sigma$ ) have both been derived from [58] and represent a normalised average value of the average directional tortuosities and a normalised unit of anisotropy respectively; a necessity to fairly compared anisotropy between different samples and materials. Whether or not these units are suitable in a highly structured medium such as the meniscus is still in need of further investigation, however, something of note is that the value of these parameters is dependent on the tortuosity method used. While it can be expected that  $\tau_c$  will change according to what method is used, looking at Table 3.7, it can be seen that the  $\sigma$  also changes. This is unexpected as  $\sigma$  is relative to the scale provided to it, therefore it should be expected that this value should remain consistent between the methods. It appears that  $\sigma$  decreased as less information is included about the pore space, but why this occurs is still not certain. This is not an area that is explored within [58] and is in need of a deeper investigation if the measurement is to be trusted. During this project, it was found that the anisotropy within the meniscus is actually twofold. The aforementioned orthogonal anisotropy, and the anisotropy along the Z-direction or 'orientation anisotropy' as it will hereby be regarded. Orientation anisotropy highlights the difference in topological resistance encountered, depending on what trajectory in the XY plane the path has. As Figure 3.6b shows, all the meniscus samples exhibit a preferential orientation in the range of 270-330°. Not only is this concept of preferential directions proven topologically, but this concept is also supported by the results found during the streamline analysis of V3E. Figure 3.10c observes a directional minima orientation almost identically to that of the minima found through topological tortuosity analysis. With the knowledge that the samples are all taken from the same region of the meniscus and orientated approximately parallel, this data supports the theory that perhaps entire regions of the meniscus are structured in a similar way to accomplish its function, but this requires more samples taken from varied locations to validate first.

## CFD-IA coupling

The methodology set out in this project presents a novel way of coupling tried and tested CFD methods, with modern image analysis techniques to expand upon the tools available to each separately. This has been accomplished by overlapping the data extracted from CFD simulations using STAR-CCM+ with the morphological information available in MATLAB. This project has predominantly focused on utilising the fluid velocity data extracted from CFD simulations, as this is one of the boundary conditions of the simulations and is also proportional to permeability. Reynolds number is a critical parameter in fluid modelling, describing the flow regime within a medium. It was only with the CFD-IA couple that the RE number could be approximated

everywhere throughout the sample. The results demonstrate that Re is highly inhomogeneous throughout the sample and, while there are 'global' trends that demonstrate the average Re along the flow direction, local values can vary greatly from this. Local Re at times can be significantly higher than the global average, at points an order of magnitude higher. This inhomogeneity presents a potential challenge to the assumptions made during flow calculations using PNM. It was found that by cross-referencing the equivalent pipe diameters with the distribution of velocities present in the 1.6m/s simulation, it is actually possible for turbulent flow to occur at 83 or 12000 locations depending if the average or maximum channel speed respectively is used. While this does not occur in actuality, the mere possibility of it occurring could be grounds to question the assumptions made during PNM. The primary assumption of which is that the flow within the system is laminar. To further support this claim, Figure 3.10a conveys that as fluid velocity varies, so does tortuosity. Given the many well-documented equations that relate permeability to tortuosity, we can conclude that the permeability of a medium also varies with speed. These points answer **RQ3**, many studies blindly assume fully laminar flow, without any real consideration into how accurate this is and neglect any possibility of local turbulent effects where Re number can peak above 2000. For many scenarios in the field of geosciences where wetting, diffusion and imbibition are the primary concern, this could be a safe assumption. However, the meniscus is distributing large amounts of impact force, so it is not unreasonable to expect much higher fluid velocities and pressure to be present. Ideally, a study would be launched to investigate the bio-mechanics of regular knee use, to produce a range of possible boundary conditions that could be used in both fluid modelling and mechanical testing [1, 8].

As discussed in Chapter 1, drawing meaningful conclusions from CFD simulations can be a difficult task, with CFD software offering few tools to analyse structures holistically. We have demonstrated already that local and global properties vary significantly. Therefore, it is beneficial to evaluate the values of other parameters at these local locations to determine what parameters have the most significant effect. With the CFD-IA coupling method proposed in this project, it is possible to speculate what parameters hold the most influence on fluid properties. Average stream speed, Re, diameter, connectivity, tortuosity and orientation were all plotted each other in the large correlation plot in Figure 3.11. The relationships between the parameters have been quantified using linear regression and the corresponding  $R^2$  is indicative of the strength of the relationship. The most significant relationships are as follows:

1. Re is strongly correlated to speed and diameter (to be expected as it is a function of both). However, the correlation between speed is notably higher than that of diameter, demonstrating the presence of smaller channels that maintain a significantly higher speed. This is reaffirmed by the speed, diameter relationship which shows a broader correlation that wider channels are generally faster, but there is an abundance of outliers to this rule.

2. Tortuosity was seen to be strongly related to speed, and streams of lower tortuosity were generally seen to be faster. This correlation is not reflected in the orientation parameter, despite having proved there is a preferential direction in Figure 3.10b. This is a limitation of the linear regression modelling, given the polar nature of the orientation, it is not possible to capture this with a linear relationship, however, it can be seen that the highest speeds occur between 270-330°, which matches up with the preferential direction demonstrated in the aforementioned plot. This relationship would be better suited to be modelled by a quadratic function.
3. Average speed was seen to be largely independent of connectivity, demonstrating that having multiple streams converge into a single channel did not in fact increase the mass flow rate within that channel.
4. A trend was presented between the diameter and connectivity of the streams. Indicating that streams tend to converge into larger channels, what mechanism draws them into these channels is still unknown.

In response to **RQ5**, the coupling of traditional CFD methods and modern image analysis techniques can provide a bounty of results not feasibly quantifiable from either independently. We have demonstrated the ability to predict an upper and lower bound for tortuosity, whilst also validating fluid orientation in fibrously structured media. We have also demonstrated potential limitations with current assumptions used during PNM and that boundary conditions should be considered before treating the results as fact. The use of PNM has however allowed for the statistical analysis of the fluid streamlines, creating the possibility to speculate the relationship between fluid flow properties without extensive simplifications about the pore space being made [72]. While this statistical analysis is still crude in its results and depth, it is an excellent starting point to build from and draw intuitive conclusions from.

## Concluding remarks

To briefly summarise the points made from the outcomes of this project and answer the research questions posed at the beginning of this project. While the current knowledge base of studies investigating the use of PNM for characterising biological media is lacking. This project, along with other studies, has derived meaningful and significant results through the methods of PNM (**RQ1**). If intending to use PNM for the characterisation of biological materials then the scope of the project should be considered when selecting a segmentation method. There is not a single 'silver bullet' solution that fits all desired outcomes, features such as computation time, accuracy, homogeneity and more are all reliant on segmentation (**RQ2**). Current research suffers from a distinct lack of standards when it comes to describing, testing and validating the various techniques employed during the PNE process. The field would benefit from an

extensive literature review addressing these questions, improving the opportunity for users with less experience or resources to utilise the methods more effectively. This lack of standardisation is prevalent in other areas of pore space characterisation as well, current literature highlights the ambiguity of definitions and methods relating to tortuosity [53]. This project has reviewed three different methods of determining tortuosity, two of which have already been investigated in depth (VC, SKL) and one of which has not (PNM). The results have found that each of the methods produces a diverse range of results and that these results are also dependent on parameters set within the method, for example, voxel connectivity or MA creation algorithm. With the parameters set in this project, it was found that the hydraulic tortuosity found from CFD simulations fell between VC and SKL geometric tortuosities (**RQ4**). When evaluating the tortuosity in all orthogonal directions, it was found that the meniscus contains a structure that is almost isotropic in the X & Y-directions, while the Z-direction presents a structure with significantly less topological resistance relative to the other directions, concluding that the structure is in fact anisotropic. The project challenges the validity of current measures of anisotropy [58] by demonstrating that these values are dependent on the method of tortuosity used. This anisotropy was also found to be twofold, an orientation analysis investigating the effect of the trajectory of a path on the tortuosity revealed that paths orientated within a range of 270-330° consistently had lower tortuosities. This hypothesis was also verified using CFD-IA coupling, with streamlines presenting the same preferential directions. CFD-IA analysis also demonstrated the variance in local and global values of flow properties through the meniscus. This variation has posed the question about the potential limitations of the assumptions made during PNM, provided that turbulent flow is feasible within the ranges testing, this would invalidate the primary assumption that allows for the prediction of fluid flow properties, making it unsuitable for analysis **RQ3**. It is suggested that an investigation into the potential boundary conditions of normal knee use should be conducted to validate or invalidate the use of PNM to predict flow properties in the meniscus. In order to try and quantify the complex interaction between fluid properties and morphology of the pore space, CFD-IA was combined with linear regression modelling to provide statistically measurable correlations. The results found that alone, none of the parameters tested revealed a dominating ( $R^2 \geq 0.9$ ) influence over the fluid velocity. Tortuosity was seen to have the highest correlation with a  $R^2$  of 0.66 which is intuitively logical. The low correlation between average channel diameter and speed also implies that the system can not be modelled using standard Bernoulli principles and that the complicated interactions between parameters need further investigation. The numerous results mentioned here answer **RQ5** as this project clearly demonstrate the ability of CFD-IA coupling to produce meaningful results. Finally, to answer **RQ6**, it is difficult to state with absolute certainty that the information we have collated is definitive proof of how the meniscus is structured to accomplish its function. What we can say for certain, is that topologically speaking, the meniscus is anisotropic in a single orthogonal direction which provides significantly less resistance to fluid flow. Within

this low-resistance flow direction are channels which offer even lower resistance. Given that all the samples analysed were extracted from the same region of the meniscus, at a similar orientation and all these preferential directions all fall within a range of  $60^\circ$ , it can be suggested that these channels do contribute towards the larger function of the meniscus. What this contribution could be is we still cannot be certain. While the CFD-IA analysis has demonstrated that these channels do have an effect on fluid flow properties, there is still a variety of other functions these structures could accomplish outside of fluid flow, such as tensile loading or stress distribution to name a few. Despite the lack of definitive answers, the innovative discoveries made by this project yield an advancement in the understanding of the obscure function of this complicated material and provide multiple avenues to build upon.

## Future Work

Throughout this project, there have been multiple suggestions made on which areas of research can be improved. The investigation into segmentation methods presented in this project only scratches the surface of PNM and the information that a comprehensive literature review and investigation into the effects of pre-processing, filtering and other PNE techniques could be of significant value to the greater community. This study has used the PNE techniques developed in order to characterise the pore space of the meniscus, however, the arguably more important phase of the meniscus is not the fluid phase, but the material phase. We have explained the structure formed from the empty spaces in the collagen, but no thought has been invested into explaining how these structures are formed to begin with. Tissue growth models could help rationalise how the meniscus is constructed to achieve its function. If the mechanisms that guide this growth process can be understood, then these mechanisms can also be used to identify and diagnose defective characteristics in patients. In the same vein of defective characteristics, while this study has only been investigating the properties of healthy human menisci, understanding and quantifying damage in degenerative menisci and investigating the effect of this on mechanical response is of huge value. Segmentation has already been used in studies to help identify and locate lesions in tissue samples [78]. This along with other modern approaches could help in the diagnosis of meniscal damage and aid in treatment[79]. As the results have shown, some segmentation methods provide more advantageous parameter distributions for use in solid-body modelling. While this is helpful to consider, the bespoke algorithm designed for use in the creation of solid-body geometry could be improved with the inclusion of final steps to eliminate the possibility of overlapping pore geometry. The final steps could include relocating pore centres or using methods to locate the overlap volumes and remove them to avoid collisions. After this algorithm has been improved, the next logical step is to explore techniques to fabricate these models. From here two schools of thought can be considered, fabrication using cheap, readily available materials and equipment such as 3D printing with plastic silicone [80]. Alternatively, samples could be constructed

using bio-polymers [81], while this is far more restrictive due to equipment, material costs and the short life span of samples, The potential information that these samples could provide would be invaluable as mechanical testing with bio-polymers is still a novel field of research. An alternative to bridging the gap between mechanical and fluid properties may not need to involve physical testing, Fluid-Structure Interaction (FSI) is a rising field of research and has already seen some usage in other materials. Creating FSI models may also be more accessible for others hoping to model materials as it requires significantly fewer resources than physical modelling. Current studies investing in FSI modelling in biological systems are scarce, with modern papers truly pioneering the way for others [82].

# Chapter 5

## Appendix

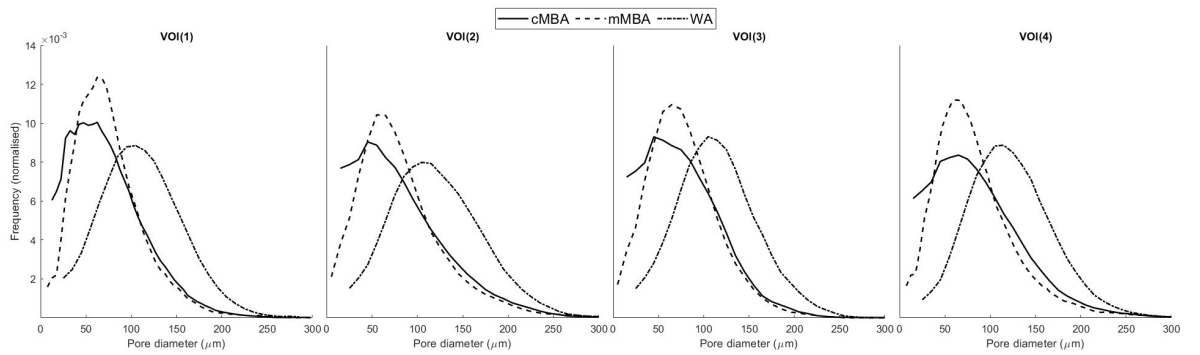


Figure 5.1: Pore-size based on segmentation method

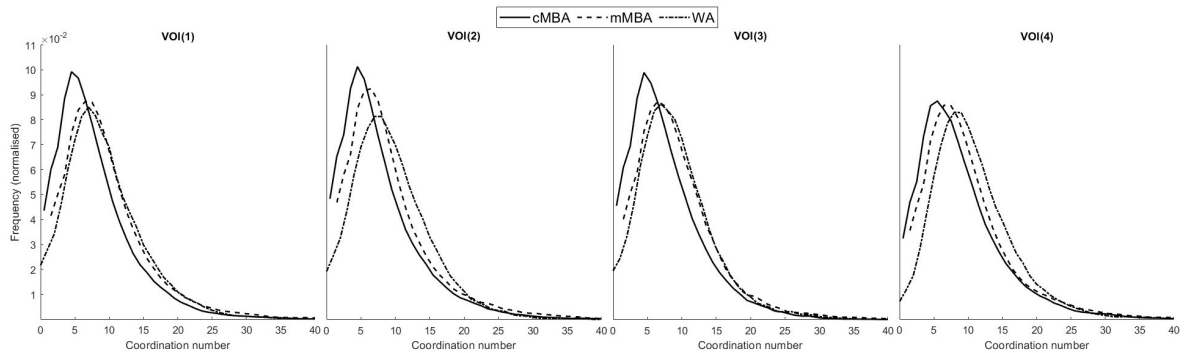


Figure 5.2: Connectivity based on segmentation method

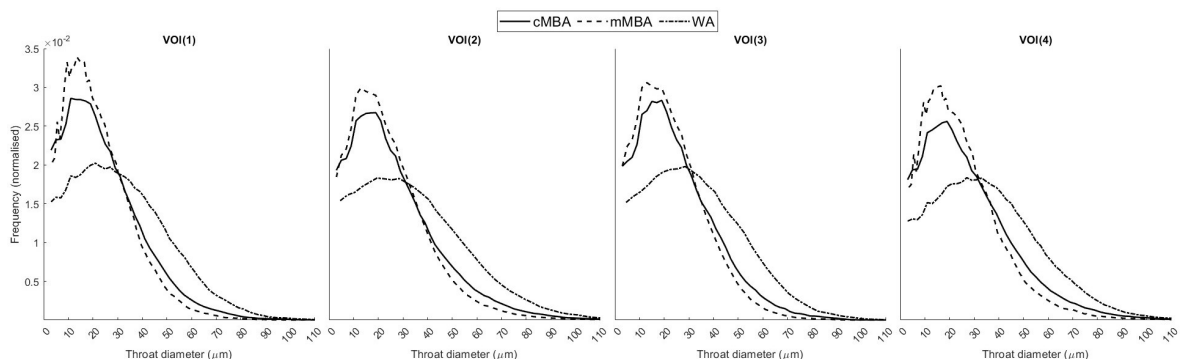


Figure 5.3: Throat-size based on segmentation method

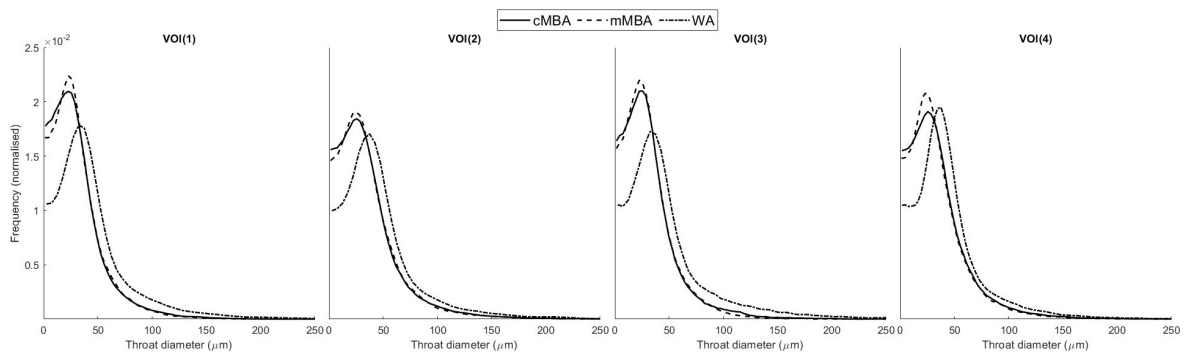


Figure 5.4: Throat length based on segmentation method

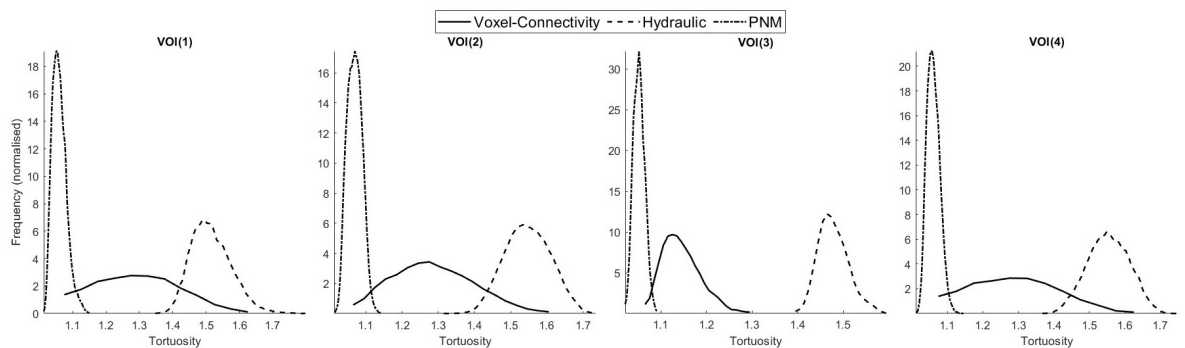


Figure 5.5: Tortuosity methodology comparison

Sample	Resolution ( $\mu\text{m}$ )	No. Pores		No. Throats		Avg. Pore Diameter ( $\mu\text{m}$ )		Avg. Throat Diameter ( $\mu\text{m}$ )		Avg. Throat Length ( $\mu\text{m}$ )		Avg. Coordination Number		Tortuosity							
		cMBA	mMBA	WA	cMBA	mMBA	WA	cMBA	mMBA	WA	cMBA	mMBA	WA								
Berea	5.35	19.6	7185	5533	3893	9999	10324	5166	56.54	67.03	76.97	40.39	39.71	47.37	94.44	114.71	133.56	2.78	3.73	2.65	-
C1	2.85	23.3	3276	1842	2053	4325	4793	2787	33.90	48.01	48.07	27.73	29.01	39.75	69.05	98.31	88.34	2.64	5.20	2.72	-
C2	5.35	16.8	5828	2242	3704	6584	5995	3382	51.91	77.85	66.82	40.91	45.76	55.39	91.91	165.06	127.09	2.26	5.35	1.83	-
S1	8.68	14.1	2144	1513	1246	2486	2499	1291	93.43	115.31	123.02	67.91	67.49	76.67	156.88	206.58	224.02	2.32	3.30	2.07	-
S2	4.96	24.6	2582	2148	1513	4464	4460	2883	62.21	72.13	84.04	43.25	42.07	49.31	104.16	113.74	135.37	3.46	4.15	3.81	-
S3	9.10	16.9	7008	1523	4180	6551	4227	2369	68.91	110.27	85.21	49.82	62.00	51.27	99.68	255.32	150.09	1.87	5.55	1.13	-
S4	8.96	17.1	7951	201	4699	7057	653	2444	66.20	162.79	81.93	48.65	91.10	48.97	93.60	481.75	143.06	1.78	6.50	1.04	-
S5	4.00	21.1	562	477	374	857	872	599	68.07	81.15	51.66	50.81	70.03	134.35	141.99	161.98	3.05	3.66	3.20	-	
S6	5.10	24	610	536	406	1041	1097	739	79.72	96.21	119.70	59.68	60.24	87.79	167.51	175.36	201.53	3.41	4.09	3.64	-
S7	4.80	25.1	1351	1253	808	2553	2715	1765	70.21	78.11	98.99	48.26	46.56	58.19	129.92	131.39	158.89	3.78	4.33	4.37	-
S8	4.89	34	1656	1645	1135	3980	4436	3095	78.93	84.14	103.52	53.00	49.23	62.90	135.17	133.43	153.34	4.81	5.39	5.45	-
Estallades	3.30	12.2	2520	2103	1635	3969	4171	2870	47.90	55.67	66.41	35.10	34.59	45.25	81.60	93.48	96.51	3.15	3.97	3.51	-
Bentheimer	3.00	21.6	1224	16900	754	-	-	-	-	-	-	-	-	-	-	-	-	-	-	-	-
F8	5.70	8.6	-	-	-	-	-	-	-	-	-	-	-	-	-	-	-	-	-	2.13	-
F10	5.70	10.2	-	-	-	-	-	-	-	-	-	-	-	-	-	-	-	-	-	1.99	-
F13	5.70	12.6	-	-	-	-	-	-	-	-	-	-	-	-	-	-	-	-	-	1.69	-
F15	5.70	15.4	-	-	-	-	-	-	-	-	-	-	-	-	-	-	-	-	-	1.63	-
F18	5.70	17.6	-	-	-	-	-	-	-	-	-	-	-	-	-	-	-	-	-	1.47	-

Table 5.1: Property table of rock paramters calculated using PNM

# Bibliography

- [1] Elsiddig Elmukashfi, Gregorio Marchiori, Matteo Berni, Giorgio Cassolas, Nicola Francesco Lopomo, Hussein Rappel, Mark Girolami, and Olga Barrera. Chapter five - model selection and sensitivity analysis in the biomechanics of soft tissues: A case study on the human knee meniscus. volume 55 of *Advances in Applied Mechanics*, pages 425–511. Elsevier, 2022. doi: <https://doi.org/10.1016/bs.aams.2022.05.001>. URL <https://www.sciencedirect.com/science/article/pii/S0065215622000023>.
- [2] H. Pereira, J. Silva-Correia, J. M. Oliveira, R. L. Reis, and J. Espregueira-Mendes. The meniscus: Basic science, 4 2013.
- [3] Alice J.S. Fox, Asheesh Bedi, and Scott A. Rodeo. The basic science of human knee menisci: Structure, composition, and function. *Sports Health*, 4:340–351, 7 2012. ISSN 19417381. doi: 10.1177/1941738111429419.
- [4] M. Khoshgoftar, A. C.T. Vrancken, T. G. van Tienen, P. Buma, D. Janssen, and N. Verdonschot. The sensitivity of cartilage contact pressures in the knee joint to the size and shape of an anatomically shaped meniscal implant. *Journal of Biomechanics*, 48:1427–1435, 6 2015. ISSN 18732380. doi: 10.1016/j.jbiomech.2015.02.034.
- [5] Asheesh Bedi, Natalie H Kelly, Michael Baad, Alice J S Fox, Robert H Brophy, Russell F Warren, and Suzanne A Maher. Dynamic contact mechanics of the medial meniscus as a function of radial tear, repair, and partial meniscectomy. *J. Bone Joint Surg. Am.*, 92(6):1398–1408, June 2010.
- [6] Greta Agustoni, Jared Maritz, James Kennedy, Francesco P. Bonomo, Stéphane P.A. Bordas, and Olga Barrera. High resolution micro-computed tomography reveals a network of collagen channels in the body region of the knee meniscus. *Annals of Biomedical Engineering*, 49:2273–2281, 9 2021. ISSN 15739686. doi: 10.1007/s10439-021-02763-6.
- [7] V. Vetri, K. Dragnevsk, M. Tkaczyk, M. Zingales, G. Marchiori, N.F. Lopomo, S. Zaffagnini, A. Bondi, J.A. Kennedy, D.W. Murray, and O Barrera. Advanced microscopy analysis of the micro-nanoscale architecture of human menisci. *Scientific Reports*, 9, 2019. doi: <https://doi.org/10.1038/s41598-019-55243-2>.

- [8] Jared Maritz, Greta Agustoni, Kalin Dragnevski, Stéphane Bordas, and Olga Barrera. The functionally grading elastic and viscoelastic properties of the body region of the knee meniscus. *Annals of Biomedical Engineering*, 49(9):2421–2429, 2021.
- [9] J. Waghorne, O. Barrera, and E.ELMUKASHFI. Biaxial mechanical testing of meniscal tissue sample. *To be submitted to Nature Materials*, 2023.
- [10] Francesco P Bonomo, Jonathan JS Gregory, and Olga Barrera. A procedure for slicing and characterizing soft heterogeneous and irregular-shaped tissue. *Materials Today: Proceedings*, 33, 2020.
- [11] Jared Maritz, Francesca Murphy, Kalin Dragnevski, and Olga Barrera. Development and optimisation of micromechanical testing techniques to study the properties of meniscal tissue. *Materials Today: Proceedings*, 33:1954–1958, 2020.
- [12] Raphaël Bulle, Gioacchino Alotta, Gregorio Marchiori, Matteo Berni, Nicola F Lopomo, Stefano Zaffagnini, Stéphane PA Bordas, and Olga Barrera. The human meniscus behaves as a functionally graded fractional porous medium under confined compression conditions. *Applied Sciences*, 11(20):9405, 2021.
- [13] Gaurav J Shah and Metin Sitti. Modeling and design of biomimetic adhesives inspired by gecko foot-hairs. In *2004 IEEE International Conference on Robotics and Biomimetics*, pages 873–878. IEEE, 2004.
- [14] Katia Zolotovsky, Swati Varshney, Steffen Reichert, Eric M Arndt, Ming Dao, Mary C Boyce, and Christine Ortiz. Fish-inspired flexible protective material systems with anisotropic bending stiffness. *Communications Materials*, 2(1):1–10, 2021.
- [15] Saikat Das, Patrick Heasman, Teng Ben, and Shilun Qiu. Porous organic materials: Strategic design and structure–function correlation. *Chemical Reviews*, 117(3):1515–1563, 2017. doi: 10.1021/acs.chemrev.6b00439. URL <https://doi.org/10.1021/acs.chemrev.6b00439>. PMID: 28035812.
- [16] M. Majewski, Habelt Susanne, and Steinbrück Klaus. Epidemiology of athletic knee injuries: A 10-year study. *The Knee*, 13(3):184–188, June 2006. doi: 10.1016/j.knee.2006.01.005. URL <https://doi.org/10.1016/j.knee.2006.01.005>.
- [17] David T. Felson, Allan Naimark, Jennifer Anderson, Lewis Kazis, William Castelli, and Robert F. Meenan. The prevalence of knee osteoarthritis in the elderly. the framingham osteoarthritis study. *Arthritis & Rheumatism*, 30(8):914–918, August 1987. doi: 10.1002/art.1780300811. URL <https://doi.org/10.1002/art.1780300811>.
- [18] T Brindle, J Nyland, and D L Johnson. The meniscus: review of basic principles with application to surgery and rehabilitation. *J. Athl. Train.*, 36(2):160–169, April 2001.

- [19] P. J. Bárto, C. K. Chua, H. A. Almeida, S. M. Chou, and A. S. C. Lim. Biomanufacturing for tissue engineering: Present and future trends. *Virtual and Physical Prototyping*, 4(4):203–216, December 2009. doi: 10.1080/17452750903476288. URL <https://doi.org/10.1080/17452750903476288>.
- [20] Tiago Ramos and Lorenzo Moroni. Tissue engineering and regenerative medicine 2019: The role of biofabrication—a year in review. *Tissue Engineering Part C: Methods*, 26(2):91–106, February 2020. doi: 10.1089/ten.tec.2019.0344. URL <https://doi.org/10.1089/ten.tec.2019.0344>.
- [21] Robert H. Brophy and Matthew J. Matava. Surgical options for meniscal replacement. *Journal of the American Academy of Orthopaedic Surgeons*, 20(5):265–272, May 2012. doi: 10.5435/jaaos-20-05-265. URL <https://doi.org/10.5435/jaaos-20-05-265>.
- [22] Flavia Libonati, Serena Graziosi, Federico Ballo, Marco Mognato, and Giacomo Sala. 3d-printed architected materials inspired by cubic bravais lattices. *ACS Biomaterials Science & Engineering*.
- [23] Rui Song, Yao Wang, Shuyu Sun, and Jianjun Liu. Characterization and microfabrication of natural porous rocks: From micro-ct imaging and digital rock modelling to micro-3d-printed rock analogs. *Journal of Petroleum Science and Engineering*, 205:108827, 2021. ISSN 0920-4105. doi: <https://doi.org/10.1016/j.petrol.2021.108827>. URL <https://www.sciencedirect.com/science/article/pii/S0920410521004885>.
- [24] Agnese Piovesan, Clement Achille, Rob Ameloot, Bart Nicolai, and Pieter Verboven. Pore network model for permeability characterization of three-dimensionally-printed porous materials for passive microfluidics. *Phys. Rev. E*, 99:033107, Mar 2019. doi: 10.1103/PhysRevE.99.033107. URL <https://link.aps.org/doi/10.1103/PhysRevE.99.033107>.
- [25] Per Valvatne, Mohammad Piri, Xavier Lopez, and Martin Blunt. Predictive pore-scale modeling of single and multiphase flow. *Transport in Porous Media*, 58:23–41, 02 2005. doi: 10.1007/s11242-004-5468-2.
- [26] A. Rabbani, A. M. Fernando, R. Shams, A. Singh, P. Mostaghimi, and M. Babaei. Review of data science trends and issues in porous media research with a focus on image-based techniques. *Water Resources Research*, 57(10):e2020WR029472, 2021. doi: <https://doi.org/10.1029/2020WR029472>. URL <https://agupubs.onlinelibrary.wiley.com/doi/abs/10.1029/2020WR029472>. e2020WR029472 2020WR029472.
- [27] Qingrong Xiong, Todor G. Baychev, and Andrey P. Jivkov. Review of pore network modelling of porous media: Experimental characterisations, network constructions and applications to reactive transport. *Journal of Contaminant Hydrol-*

- ogy*, 192:101–117, 2016. ISSN 0169-7722. doi: <https://doi.org/10.1016/j.jconhyd.2016.07.002>. URL <https://www.sciencedirect.com/science/article/pii/S016977221630122X>.
- [28] Martin J. Blunt, Branko Bijeljic, Hu Dong, Oussama Gharbi, Stefan Iglauer, Peyman Mostaghimi, Adriana Paluszny, and Christopher Pentland. Pore-scale imaging and modelling. *Advances in Water Resources*, 51:197–216, 2013. ISSN 0309-1708. doi: <https://doi.org/10.1016/j.advwatres.2012.03.003>. URL <https://www.sciencedirect.com/science/article/pii/S0309170812000528>. 35th Year Anniversary Issue.
- [29] Tom Bultreys, Wesley De Boever, and Veerle Cnudde. Imaging and image-based fluid transport modeling at the pore scale in geological materials: A practical introduction to the current state-of-the-art. *Earth-Science Reviews*, 155:93–128, 2016. ISSN 0012-8252. doi: <https://doi.org/10.1016/j.earscirev.2016.02.001>. URL <https://www.sciencedirect.com/science/article/pii/S0012825216300150>.
- [30] Linxian Gong, Lei Nie, and Yan Xu. Geometrical and topological analysis of pore space in sandstones based on x-ray computed tomography. *Energies*, 13, 8 2020. ISSN 19961073. doi: 10.3390/en13153774.
- [31] Priyanka Agrawal, Arjen Mascini, Tom Bultreys, Hamed Aslannejad, Mariëtte Wolthers, Veerle Cnudde, Ian B. Butler, and Amir Raoof. The impact of pore-throat shape evolution during dissolution on carbonate rock permeability: Pore network modeling and experiments. *Advances in Water Resources*, 155:103991, September 2021. doi: 10.1016/j.advwatres.2021.103991. URL <https://doi.org/10.1016/j.advwatres.2021.103991>.
- [32] Bagus P. Muljadi, Martin J. Blunt, Ali Q. Raeini, and Branko Bijeljic. The impact of porous media heterogeneity on non-darcy flow behaviour from pore-scale simulation. *Advances in Water Resources*, 95:329–340, September 2016. doi: 10.1016/j.advwatres.2015.05.019. URL <https://doi.org/10.1016/j.advwatres.2015.05.019>.
- [33] Arash Rabbani and Masoud Babaei. Hybrid pore-network and lattice-boltzmann permeability modelling accelerated by machine learning. *Advances in Water Resources*, 126:116–128, 2019. ISSN 0309-1708. doi: <https://doi.org/10.1016/j.advwatres.2019.02.012>. URL <https://www.sciencedirect.com/science/article/pii/S0309170818311059>.
- [34] Jianlin Zhao, Feifei Qin, Dominique Derome, Qinjun Kang, and Jan Carmeliet. Improved pore network models to simulate single-phase flow in porous media by coupling with lattice boltzmann method. *Advances in Water Resources*, 145:103738, 2020. ISSN 0309-1708. doi: <https://doi.org/10.1016/j.advwatres.2020.103738>.

- 2020.103738. URL <https://www.sciencedirect.com/science/article/pii/S0309170820307533>.
- [35] Hu Dong and Martin J. Blunt. Pore-network extraction from micro-computerized-tomography images. *Physical Review E - Statistical, Nonlinear, and Soft Matter Physics*, 80, 9 2009. ISSN 15393755. doi: 10.1103/PhysRevE.80.036307.
  - [36] Jeff T. Gostick. Versatile and efficient pore network extraction method using marker-based watershed segmentation. *Phys. Rev. E*, 96:023307, Aug 2017. doi: 10.1103/PhysRevE.96.023307. URL <https://link.aps.org/doi/10.1103/PhysRevE.96.023307>.
  - [37] Arash Rabbani, Saeid Jamshidi, and Saeed Salehi. An automated simple algorithm for realistic pore network extraction from micro-tomography images. *Journal of Petroleum Science and Engineering*, 123:164–171, 11 2014. ISSN 09204105. doi: 10.1016/j.petrol.2014.08.020.
  - [38] Todor G. Baychev, Andrey P. Jivkov, Arash Rabbani, Ali Q. Raeini, Qingrong Xiong, Tristan Lowe, and Philip J. Withers. Reliability of algorithms interpreting topological and geometric properties of porous media for pore network modelling. *Transport in Porous Media*, 128(1):271–301, March 2019. doi: 10.1007/s11242-019-01244-8. URL <https://doi.org/10.1007/s11242-019-01244-8>.
  - [39] J. Waghorne, C. Howard, H. Hu, J. Pang, W. J. Peveler, L. Harris, and O. Barrera. The applicability of transperceptual and deep learning approaches to the study and mimicry of complex cartilaginous tissues. *arXiv e-prints*, art. arXiv:2211.14314, November 2022.
  - [40] Zhongzheng Wang, Hyogu Jeong, Yixiang Gan, Jean-Michel Pereira, Yuantong Gu, and Emilie Sauret. Pore-scale modeling of multiphase flow in porous media using a conditional generative adversarial network (cgan). *Physics of Fluids*, 34(12):123325, 2022. doi: 10.1063/5.0133054. URL <https://doi.org/10.1063/5.0133054>.
  - [41] Mariane Barsi-Andreeta, Everton Lucas-Oliveira, Arthur Gustavo de Araujo-Ferreira, Willian Andriguetto Trevizan, and Tito José Bonagamba. Pore network and medial axis simultaneous extraction through maximal ball algorithm. 12 2019. URL <http://arxiv.org/abs/1912.04759>.
  - [42] Zhixing Yi, Mian Lin, Wenbin Jiang, Zhaobin Zhang, Haishan Li, and Jian Gao. Pore network extraction from pore space images of various porous media systems. *Water Resources Research*, 53:3424–3445, 4 2017. ISSN 19447973. doi: 10.1002/2016WR019272.
  - [43] Frederick Arand and Jürgen Hesser. Accurate and efficient maximal ball algorithm for pore network extraction. *Computers and Geosciences*, 101:28–37, 4 2017. ISSN 00983004. doi: 10.1016/j.cageo.2017.01.004.

- [44] A. Amankwah and C. Aldrich. Rock image segmentation using watershed with shape markers. In *2010 IEEE 39th Applied Imagery Pattern Recognition Workshop (AIPR)*, pages 1–7, 2010. doi: 10.1109/AIPR.2010.5759719.
- [45] Kirill M. Gerke, Timofey O. Sizonenko, Marina V. Karsanina, Efim V. Lavrukhin, Vladimir V. Abashkin, and Dmitry V. Korost. Improving watershed-based pore-network extraction method using maximum inscribed ball pore-body positioning. *Advances in Water Resources*, 140, 6 2020. ISSN 03091708. doi: 10.1016/j.advwatres.2020.103576.
- [46] Jun Guo, Qing Hu, Yuan Yao, Qi Lu, Yong Yu, and yi Qian. A pore network model based method for tissue engineering scaffold design. pages 1 – 4, 05 2010. doi: 10.1109/ICBECS.2010.5462518.
- [47] Imperial College London. Micro-ct images and networks, 2007. URL <https://www.imperial.ac.uk/earth-science/research/research-groups/pore-scale-modelling/micro-ct-images-and-networks>.
- [48] Hu Dong and Martin J Blunt. Pore-network extraction from micro-computerized-tomography images. *Physical review E*, 80(3):036307, 2009.
- [49] Carl Fredrik Berg and Rudolf Held. Fundamental transport property relations in porous media incorporating detailed pore structure description. *Transport in Porous Media*, 112(2):467–487, 2016.
- [50] Jinlong Fu, Hywel R. Thomas, and Chenfeng Li. Tortuosity of porous media: Image analysis and physical simulation. *Earth-Science Reviews*, 212: 103439, 2021. ISSN 0012-8252. doi: <https://doi.org/10.1016/j.earscirev.2020.103439>. URL <https://www.sciencedirect.com/science/article/pii/S0012825220304852>.
- [51] Bernhard Tjaden, Samuel J Cooper, Daniel JL Brett, Denis Kramer, and Paul R Shearing. On the origin and application of the bruggeman correlation for analysing transport phenomena in electrochemical systems. *Current Opinion in Chemical Engineering*, 12:44–51, May 2016. doi: 10.1016/j.coche.2016.02.006. URL <https://doi.org/10.1016/j.coche.2016.02.006>.
- [52] Faruk Civan. Effective correlation of apparent gas permeability in tight porous media. *Transport in Porous Media*, 82(2):375–384, July 2009. doi: 10.1007/s11242-009-9432-z. URL <https://doi.org/10.1007/s11242-009-9432-z>.
- [53] Behzad Ghanbarian, Allen G. Hunt, Robert P. Ewing, and Muhammad Sahimi. Tortuosity in porous media: A critical review. *Soil Science Society of America Journal*, 77:1461–1477, 9 2013. ISSN 03615995. doi: 10.2136/sssaj2012.0435.
- [54] Yu Bo-Ming and Li Jian-Hua. A geometry model for tortuosity of flow path in porous media. *Chinese Physics Letters*, 21(8):1569, aug 2004. doi: 10.1088/

- 0256-307X/21/8/044. URL <https://dx.doi.org/10.1088/0256-307X/21/8/044>.
- [55] Wojciech Sobieski. The use of path tracking method for determining the tortuosity field in a porous bed. *Granular Matter*, 18, 8 2016. ISSN 14347636. doi: 10.1007/s10035-016-0668-3.
  - [56] Yu San Wu, Lucas J. van Vliet, Henderik W. Frijlink, and Kees van der Voort Maarschalk. The determination of relative path length as a measure for tortuosity in compacts using image analysis. *European Journal of Pharmaceutical Sciences*, 28:433–440, 8 2006. ISSN 09280987. doi: 10.1016/j.ejps.2006.05.006.
  - [57] Peijun Guo. Lower and upper bounds for hydraulic tortuosity of porous materials. *Transport in Porous Media*, 109:659–671, 10 2015. ISSN 01693913. doi: 10.1007/s11242-015-0541-6.
  - [58] S.J. Cooper, D.S. Eastwood, J. Gelb, G. Damblanc, D.J.L. Brett, R.S. Bradley, P.J. Withers, P.D. Lee, A.J. Marquis, N.P. Brandon, and P.R. Shearing. Image based modelling of microstructural heterogeneity in lifepo<sub>4</sub> electrodes for li-ion batteries. *Journal of Power Sources*, 247:1033–1039, 2014. ISSN 0378-7753. doi: <https://doi.org/10.1016/j.jpowsour.2013.04.156>. URL <https://www.sciencedirect.com/science/article/pii/S0378775313007763>.
  - [59] Francis AL Dullien. *Porous media: fluid transport and pore structure*. Academic press, 2012.
  - [60] Helge K. Dahle, Michael A. Celia, and S. Majid Hassanzadeh. *Bundle-of-Tubes Model for Calculating Dynamic Effects in the Capillary-Pressure-Saturation Relationship*, pages 5–22. Springer Netherlands, Dordrecht, 2005. ISBN 978-1-4020-3604-0. doi: 10.1007/1-4020-3604-3\_2. URL [https://doi.org/10.1007/1-4020-3604-3\\_2](https://doi.org/10.1007/1-4020-3604-3_2).
  - [61] D Bauer, S Youssef, M Fleury, S Bekri, E Rosenberg, and O Vizika. Improving the estimations of petrophysical transport behavior of carbonate rocks using a dual pore network approach combined with computed microtomography. *Transport in porous media*, 94(2):505–524, 2012.
  - [62] *Fluid Coupling in the Combined Finite-Discrete Element Method*, chapter 8, pages 255–276. John Wiley Sons, Ltd, 2004. ISBN 9780470020180. doi: <https://doi.org/10.1002/0470020180.ch8>. URL <https://onlinelibrary.wiley.com/doi/abs/10.1002/0470020180.ch8>.
  - [63] Clara Sandino, Paul Kroliczek, David D. McErlain, and Steven K. Boyd. Predicting the permeability of trabecular bone by micro-computed tomography and finite element modeling. *Journal of Biomechanics*, 47(12):3129–3134, 2014. ISSN 0021-9290. doi: <https://doi.org/10.1016/j.jbiomech.2014.06.024>. URL <https://www.sciencedirect.com/science/article/pii/S0021929014003637>.

- [64] Edo S. Boek and Maddalena Venturoli. Lattice-boltzmann studies of fluid flow in porous media with realistic rock geometries. *Computers Mathematics with Applications*, 59(7):2305–2314, 2010. ISSN 0898-1221. doi: <https://doi.org/10.1016/j.camwa.2009.08.063>. URL <https://www.sciencedirect.com/science/article/pii/S0898122109006427>. Mesoscopic Methods in Engineering and Science.
- [65] M.L. Stewart, A.L. Ward, and D.R. Rector. A study of pore geometry effects on anisotropy in hydraulic permeability using the lattice-boltzmann method. *Advances in Water Resources*, 29(9):1328–1340, 2006. ISSN 0309-1708. doi: <https://doi.org/10.1016/j.advwatres.2005.10.012>. URL <https://www.sciencedirect.com/science/article/pii/S0309170805002514>.
- [66] Ying Da Wang, Traiwit Chung, Arash Rabbani, Ryan T. Armstrong, and Peyman Mostaghimi. Fast direct flow simulation in porous media by coupling with pore network and laplace models. *Advances in Water Resources*, 150:103883, 2021. ISSN 0309-1708. doi: <https://doi.org/10.1016/j.advwatres.2021.103883>. URL <https://www.sciencedirect.com/science/article/pii/S0309170821000385>.
- [67] Jack Waghorne. Pne extarction algoirthms, msc by research 2022, 2022. URL <https://github.com/Jack-Waghorne/meniscal-pm/tree/main/pnm%20algorithms>.
- [68] *Robust Determination of the Pore Space Morphology in Sedimentary Rocks*, volume All Days of SPE Annual Technical Conference and Exhibition, 10 2003. doi: 10.2118/84296-MS. URL <https://doi.org/10.2118/84296-MS>. SPE-84296-MS.
- [69] C.R. Maurer, Rensheng Qi, and V. Raghavan. A linear time algorithm for computing exact euclidean distance transforms of binary images in arbitrary dimensions. *IEEE Transactions on Pattern Analysis and Machine Intelligence*, 25(2):265–270, 2003. doi: 10.1109/TPAMI.2003.1177156.
- [70] T.C. Lee, R.L. Kashyap, and C.N. Chu. Building skeleton models via 3-d medial surface axis thinning algorithms. *CVGIP: Graphical Models and Image Processing*, 56(6):462–478, 1994. ISSN 1049-9652. doi: <https://doi.org/10.1006/cgip.1994.1042>. URL <https://www.sciencedirect.com/science/article/pii/S104996528471042X>.
- [71] Yuntao Liang, Peiyu Hu, Shugang Wang, Shuanglin Song, and Shuang Jiang. Medial axis extraction algorithm specializing in porous media. *Powder Technology*, 343:512–520, 2019. ISSN 0032-5910. doi: <https://doi.org/10.1016/j.powtec.2018.11.061>. URL <https://www.sciencedirect.com/science/article/pii/S0032591018309653>.
- [72] Kai Xu, Wei Wei, Yin Chen, Haitao Tian, Sai Xu, and Jianchao Cai. A pore network approach to study throat size effect on the permeability of reconstructed

- porous media. *Water*, 14(1), 2022. ISSN 2073-4441. doi: 10.3390/w14010077. URL <https://www.mdpi.com/2073-4441/14/1/77>.
- [73] Eric W Weisstein. Sphere-sphere intersection, 2007. URL <https://mathworld.wolfram.com/Sphere-SphereIntersection.html>.
- [74] Michael Kerschnitzki, Philip Kollmannsberger, Manfred Burghammer, Georg N Duda, Richard Weinkamer, Wolfgang Wagermaier, and Peter Fratzl. Architecture of the osteocyte network correlates with bone material quality. *Journal of Bone and Mineral Research*, 28(8):1837–1845, 2013. doi: <https://doi.org/10.1002/jbmr.1927>. URL <https://asbmrr.onlinelibrary.wiley.com/doi/abs/10.1002/jbmr.1927>.
- [75] Hanzheng Wang, Xiaohe Chen, Randy Moss, Ronald Stanley, William Stoecker, M. Emre Celebi, Thomas Szalapski, Joseph Malters, James Grichnik, Ashfaq Marghoob, Harold Rabinovitz, and Scott Menzies. Watershed segmentation of dermoscopy images using a watershed technique. *Skin research and technology : official journal of International Society for Bioengineering and the Skin (ISBS) [and] International Society for Digital Imaging of Skin (ISDIS) [and] International Society for Skin Imaging (ISSI)*, 16:378–84, 08 2010. doi: 10.1111/j.1600-0846.2010.00445.x.
- [76] Xiang Huang, Yinwu He, Wei Zhou, Daxiang Deng, and Yanwei Zhao. Pore network modeling of fibrous porous media of uniform and gradient porosity. *Powder Technology*, 343, 11 2018. doi: 10.1016/j.powtec.2018.11.022.
- [77] Mohammad Amin Sadeghi, Mahmoudreza Aghighi, Jake Barralet, and Jeff T. Gostick. Pore network modeling of reaction-diffusion in hierarchical porous particles: The effects of microstructure. *Chemical Engineering Journal*, 330:1002–1011, 2017. ISSN 1385-8947. doi: <https://doi.org/10.1016/j.cej.2017.07.139>. URL <https://www.sciencedirect.com/science/article/pii/S138589471731286X>.
- [78] Hanzheng Wang, Xiaohe Chen, Randy H. Moss, R. Joe Stanley, William V. Stoecker, M. Emre Celebi, Thomas M. Szalapski, Joseph M. Malters, James M. Grichnik, Ashfaq A. Marghoob, Harold S. Rabinovitz, and Scott W. Menzies. Watershed segmentation of dermoscopy images using a watershed technique. *Skin Research and Technology*, March 2010. doi: 10.1111/j.1600-0846.2010.00445.x. URL <https://doi.org/10.1111/j.1600-0846.2010.00445.x>.
- [79] Adeel Ahmad, Steven G. Adie, Morgan Wang, and Stephen A. Boppart. Sonification of optical coherence tomography data and images. *Opt. Express*, 18(10):9934–9944, May 2010. doi: 10.1364/OE.18.009934. URL <https://opg.optica.org/oe/abstract.cfm?URI=oe-18-10-9934>.
- [80] Eric Luis, Houwen Matthew Pan, Swee Leong Sing, Ram Bajpai, Juha Song, and Wai Yee Yeong. 3d direct printing of silicone meniscus implant using a novel heat-

- cured extrusion-based printer. *Polymers*, 12(5):1031, May 2020. doi: 10.3390/polym12051031. URL <https://doi.org/10.3390/polym12051031>.
- [81] Hao Li, Pinxue Li, Zhen Yang, Cangjian Gao, Liwei Fu, Zhiyao Liao, Tianyuan Zhao, Fuyang Cao, Wei Chen, Yu Peng, Zhiguo Yuan, Xiang Sui, Shuyun Liu, and Quanyi Guo. Meniscal regenerative scaffolds based on biopolymers and polymers: Recent status and applications. *Frontiers in Cell and Developmental Biology*, 9, July 2021. doi: 10.3389/fcell.2021.661802. URL <https://doi.org/10.3389/fcell.2021.661802>.
- [82] Matthew Hirschhorn, Vakhtang Tchantchaleishvili, Randy Stevens, Joseph Rossano, and Amy Throckmorton. Fluid–structure interaction modeling in cardiovascular medicine – a systematic review 2017–2019. *Medical Engineering & Physics*, 78:1–13, April 2020. doi: 10.1016/j.medengphy.2020.01.008. URL <https://doi.org/10.1016/j.medengphy.2020.01.008>.